Accepted Manuscript

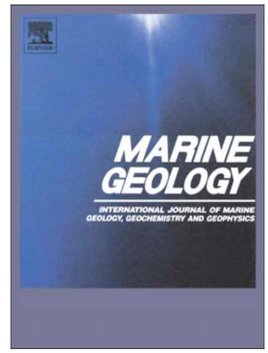

Focussed Fluid Flow on the Hikurangi Margin, New Zealand – Evidence from Possible Local Upwarping of the Base of Gas Hydrate Stability

Ingo A. Pecher, Stuart A. Henrys, Warren T. Wood, Nina Kukowski, Gareth J. Crutchley, Miko Fohrmann, Jeremy Kilner, Kim Senger, Andrew R. Gorman, Richard B. Coffin, Jens Greinert, Kevin Faure

PII: S0025-3227(09)00268-0
DOI: doi: 10.1016/j.margeo.2009.10.006
Reference: MARGO 4413

To appear in: *Marine Geology*

Received date: 13 October 2008
Revised date: 25 September 2009
Accepted date: 5 October 2009

Focussed Fluid Flow on the Hikurangi Margin, New Zealand – Evidence from Possible Local Upwarping of the Base of Gas Hydrate Stability

Special Section: Methane Seeps

Ingo A. Pecher[1]
Institute of Petroleum Engineering & ECOSSE, Heriot-Watt University, Edinburgh, EH14 4AS, UK, ingo.pecher@pet.hw.ac.uk
Tel.: +44 131 451 3675, FAX: 451 3127

Stuart A. Henrys
GNS Science, PO Box 30368, Lower Hutt, New Zealand

Warren T. Wood
Naval Research Laboratory, Stennis Space Center, MS 39529, USA

Nina Kukowski
GFZ German Research Centre for Geosciences, Telegrafenberg, 14473 Potsdam, Germany

Gareth J. Crutchley[2], Miko Fohrmann[1], Jeremy Kilner, Kim Senger[3], Andrew R. Gorman
Department of Geology, University of Otago, PO Box 56, Dunedin, New Zealand

Richard B. Coffin
Naval Research Laboratory, 4555 Overlook Avenue SW, Washington, DC 20375, USA

Jens Greinert[4]
Renard Centre of Marine Geology, Ghent University, Krijgslaan 281 s.8 B-9000 Gent, Belgium

Kevin Faure
GNS Science, PO Box 30368, Lower Hutt, New Zealand

Corresponding Author: Ingo A. Pecher

[1]Present address: GNS Science, PO Box 30368, Lower Hutt, New Zealand
[2]Present address: IfM-Geomar, Wischhofstr. 1-3, 24148 Kiel, Germany
[3]Present address: Bayerngas Norge AS, Lilleakerveien 4, N-0216 Oslo, Norway
[4]Present address: Dept. Marine Geology, Royal Netherlands Institute for Sea Research (NIOZ), PO Box 59, 1790 AB Den Burg, Texel, The Netherlands

Abstract

The southern Hikurangi subduction margin is characterized by significant accretion with predicted high rates of fluid expulsion. Bottom simulating reflections (BSRs) are widespread on this margin, predominantly occurring beneath thrust ridges. We present seismic data across the Porangahau Ridge on the outer accretionary wedge. The data show high-amplitude reflections above the regional BSR level. Based on polarity and reflection strength, we interpret these reflections as being caused by free gas. We propose the presence of gas above the regional level of BSRs indicates local upwarping of the base of gas hydrate stability caused by advective heatflow from upward migrating fluids, although we cannot entirely rule out alternative processes. Simplified modelling of the increase of the thermal gradient associated with fluid flow suggests that funnelling of upward migrating fluids beneath low-permeability slope basins into the Porangahau Ridge would not lead to the pronounced thermal anomaly inferred from upwarping of the base of gas hydrate stability. Focussing of fluid flow is predicted to take place deep in the accretionary wedge and/or the underthrust sediments. Above the high-amplitude reflections, sediment reflectivity is low. A lack of lateral continuity of reflections suggests that reflectivity is lost because of a destruction of sediment layering from deformation rather than gas-hydrate-related amplitude blanking. Structural permeability from fracturing of sediments during deformation may facilitate fluid expulsion on the ridge. A gap in the BSR in the southern part of the study area may be caused by a loss of gas during fluid expulsion. We speculate that gaps in otherwise continuous BSRs that are observed beneath some thrusts on the Hikurangi Margin may be characteristic of other locations experiencing focussed fluid expulsion.

Keywords: Fluid flow, gas hydrates, Hikurangi Margin, subduction zones

1. Introduction

Large quantities of fluids are predicted to be expelled from compacting sediments on accretionary subduction margins. Fluid expulsion is thought to be highly focussed, although the exact locations of expulsion are usually constrained on very small scales (centimetres to meters) from point measurements on the seafloor (e.g., Bohrmann et al., 2002) and in boreholes (e.g., Saffer and Screaton, 2003) and they have been predicted on regional scales (kilometres) from modelling (e.g., Kukowski and Pecher, 1999). Bottom simulating reflections (BSRs) mark the pressure-temperature conditions of the gas-hydrate phase boundary and thus, allow temperature estimates at the base of gas hydrate stability (BGHS), usually hundreds of meters beneath the seafloor (Yamano et al., 1982). Continuous lateral coverage with temperature “measurements” associated with BSRs at depths that are not affected by near-seafloor anomalies makes BSRs well suited for investigating lateral temperature anomalies on scales of tens to hundreds of meters. BSR shoaling has been successfully used to constrain fluid expulsion for example, along a fault on the Cascadia margin (Mann and Kukowski, 1999).

Gas hydrate formation appears to be closely linked to fluid flow because, in most settings, it is predicted to require supply of gas from below into the hydrate stability zone (Ruppel and Kinoshita, 2000). Models for gas hydrate formation based on single-phase fluid flow (Zatsepina and Buffett, 1997; Xu and Ruppel, 1999; Ruppel and Kinoshita, 2000; Xu, 2004) assume gas is transported into the hydrate stability zone in solution in upward migrating pore water. Gas hydrates form from gas that comes out of solution because methane solubility decreases while the fluids approach the seafloor. These models explain the relatively low levels of gas hydrate saturation in environments with relatively low fluid flux such as the Blake Ridge offshore South Carolina (Xu and Ruppel, 1999).

Recently developed two-phase models (Haeckel et al., 2004; Liu and Flemings, 2006; Liu and Flemings, 2007) predict that in regions with high gas supply, free gas may migrate into and through the gas hydrate stability zone without getting "trapped" as solid hydrate. The formation of gas hydrate is slowed down because of an increase of salinity during hydrate formation inhibiting further formation of hydrate (Liu and Flemings, 2006), kinetic effects (Haeckel et al., 2004), or limited availability of water (Ginsburg and Soloviev, 1997). Two-phase models have been invoked to explain the high concentrations of near-seafloor gas hydrate and the coexistence of free gas and hydrates on Hydrate Ridge, off Oregon (Haeckel et al., 2004; Liu and Flemings, 2006).

We present seismic data from the Porangahau Ridge, a thrust ridge on the southern Hikurangi Margin east of New Zealand, that show evidence for free gas above the regional level of BSRs. We interpret this finding as being caused by local upwarping of the BGHS from fluid expulsion, although we cannot entirely rule out alternative models.

2. Geologic Setting

Along the Hikurangi Margin, the Hikurangi Plateau, a large igneous province of the Pacific Plate, is subducted obliquely beneath the Australian Plate at a rate of ~40-45 mm/yr (DeMets et al., 1994; Figure 1). Subduction started 20-25 Ma (Ballance, 1976) and led to the formation of an accretionary wedge (Lewis and Pettinga, 1993; Barnes et al., this issue). The wedge is growing rapidly with 3 km of trench fill consisting of turbidites and mudstones being accreted at a rate of 12±3 mm/yr (Barnes and Mercier de Lepinay, 1997). A low slope angle of <1°, similar to the Barbados prism, and a basal dip of <3°, on the higher end of values for the Barbados prism (Wang and Hu, 2006), indicate a low angle of friction typical for largely uncompacted, overpressured sediments with high water content (Barnes et al., 1998; Barnes et al., this issue). The margin is highly overpressured reaching near-lithostatic pressure at about 2 km depth in near-shore and on-shore oilwells (Sibson and Rowland, 2003). It is thought that fine-grained mudstones play a significant role as caps in sustaining overpressure (Sibson and Rowland, 2003). Accretion and subduction is predicted to cause significant dewatering, which is linked to numerous vents found on land and offshore (Giggenbach et al., 1993a; Lewis and Marshall, 1996; Faure et al., 2006; Bialas et al., 2007). The geologic setting of the southern Hikurangi Margin is described in detail by Barnes et al. (this issue).

BSRs in seismic data show evidence for widespread gas hydrates on the Hikurangi Margin (Katz, 1981; Townend, 1997a; Henrys et al., 2003). BSRs on this margin are ubiquitous beneath anticlines but largely absent in the slope basins (Pecher and Henrys, 2003; Henrys et al., in press).

A seismic line (05CM-38, see Figure 1 for location) acquired with a configuration for hydrocarbon exploration across the Hikurangi Margin in 2005, revealed a prominent high-reflectivity zone above the regional level of BSRs beneath the southern Porangahau Ridge. The Porangahau Ridge (Figure 1) was subsequently one of the focus areas of *R/V Tangaroa's* CHARMNZ (CH4-Hydrates on the AccRetionary Margins of New Zealand) campaign in 2006, a New Zealand, U.S.A., and European collaboration.

The ridge is located seaward of a Cretaceous to Palaeogene foundation that is thought to act as a deforming tectonic buttress for a frontal accretionary wedge

(Lewis and Pettinga, 1993; Barnes et al., this issue). The Porangahau Ridge is underlain by mainly Plio- to Pleistocene accreted trench-fill turbidites and flanked by slope basins with Miocene to Recent sediments. Further north, the seaward edge of the Cretaceous to Palaeogene sequence is thought to be located beneath the Porangahau Ridge itself (Figure 1; Barnes et al., this issue). The décollement between overriding and subducting plate is estimated to be about 5 km beneath the Porangahau Ridge (Barnes et al., this issue).

3. Data

3.1 Acquisition and Processing

During the CHARMNZ campaign, we acquired high-resolution seismic reflection profiles, heatflow transects, pore-water chemistry profiles from piston cores, echosounder data, and water-column chemistry profiles (Pecher et al., 2007; Coffin et al., 2008a). These data were complemented in 2007 by a controlled-source electromagnetic survey (Schwalenberg et al., this issue) and additional seismic lines further to the north and south of the ridge (Barnes et al., this issue) during the NewVents project, *R/V Sonne* voyage SO191 (Bialas et al., 2007).

We present results from seismic transects acquired during the CHARMNZ cruise. The data were processed to achieve high lateral resolution. Shot gathers were FK filtered prior to common-mid-point (CMP) binning at 6.25 m. Because of the short maximum source-receiver distance compared to water depth, the moveout of the CMP gathers was not affected noticeably by seismic velocities. CMP gathers were therefore normal-moveout corrected assuming a constant velocity of 1500 m/s and stacked. Post-stack sections were finite-difference migrated and gain-corrected for spherical divergence, preserving relative amplitudes.

3.2 Seismic Images

The seismic profiles are displayed from north to south in Figure 2. CMP positions are converted to distance such that the axis of the anticline is situated at 6.25 km (Figure 1). Seismic amplitudes are normalized to the average reflection coefficient of the seafloor of 100 CMPs on either side of the plots in the slope basins, which was calculated from the amplitudes of seafloor and water-multiple arrivals. This was done to allow better comparison of the seismic images, although their appearance may still be affected by changes in streamer depth and the number of recording channels (Table 1).

The surface expression of the ridge in the northernmost line (Line P1) is only a change of slope dip, but subsurface strata are more tightly folded. Some disruptions in seafloor topography above the ridge are beyond the scope of this study. A BSR extends across the anticline. The next line to the south, Line P2, displays a relatively smooth seafloor, continuous sub-surface reflections with only a few high-amplitude patches above the BSR at about 9-10 km, and a continuous BSR.

A pattern of extensional faults appears beneath the anticline in Line P3 that can be traced almost down to the BSR. High-amplitude reflections appear >0.1 s above the BSR around 6, 8 and 11 km along the section. Sediment reflectivity decreases significantly ~0.1-0.2 s above these anomalies. We focus our analysis on the high-reflectivity zone (HRZ) at ~6 km because it reaches furthest above the BSR further south.

In Line P4, this HRZ and the overlying zone of low reflectivity expand further upwards. Extensional faults are can be traced from the seafloor into the zone of low reflectivity. The BSR beneath the high-amplitude events appears broken.

The core of the anticline breaches the seafloor between Lines P4 and P5. In Line P5, the extensional fault pattern beneath the seafloor disappears. Undulating and disturbed, “wiggly” reflections are present in the first ~0.1 s beneath the seafloor immediately west of the anticline. The HRZ expands further towards the seafloor. Otherwise, the reflectivity beneath the anticline is low.

The HRZ in Line P6 stretches more than half-way to the seafloor while the BSR beneath them has disappeared. On the western edge of the anticline, some “wiggly” reflections are present immediately beneath the seafloor. Apart from the HRZ, the BSR, and some weak reflections down to ~0.1 s beneath the seafloor, the sediment section beneath the anticline has low reflectivity.

Between Lines P6 and P7, the HRZ disappears except for a short segment above fragments of a BSR. Similar fragments of BSRs are present in Line P8 with a short high-amplitude reflection extending some 0.1 s above the BSR.

In Line P9, only sporadic reflections are present at the BSR level. Some reflections are present above the BSR level beneath the anticline. These reflections appear more continuos and weaker than the high-amplitude events in Lines P3-P6.

In summary, we observe several HRZs above the regional level of BSRs. The westernmost zone starts at Line P3, approaches the seafloor, until it disappears between Lines P6 and P7. This HRZ, assuming it is continuous from line to line, extends for ~ 6 km along the axis of the anticline. The north-to-south development of the HRZ coincides with fragmentation and partial disappearance of the BSR beneath the ridge. We also see a decrease of sediment reflectivity above the HRZ. Near-vertical faulting is present above the northern part of the HRZ whereas undulating reflections beneath the seafloor occur to the west of where the core of the anticline has breached the seafloor above the southern part of this HRZ.

3.3 Polarity of Reflections Above the Regional BSR level

We investigated whether reflections from the HRZ are caused by a decrease of seismic impedance (velocity multiplied by density) typical of gas or an increase potentially indicative of gas hydrates in the pore space. The HRZs mostly consist of discontinuous reflectivity patches, making it difficult to study their polarity. At one location however, along Line P4 around 5.9 km, a continuous reflection could be identified. The wavelet of this reflection displays negative polarity compared to the seafloor (Figure 3) indicating a significant drop of seismic impedance. Reflection strength is similar to that of the seafloor.

In Line P9, a reflection band is also present above the BSR level. The upper-most reflection has negative polarity with respect to the seafloor reflection (Figure 3). Compared to the event in Line P4, amplitudes are relatively weak and the reflections appear to form folded, continuous layers.

3.4 Nature of Reflectivity Reduction

We investigated whether the low-reflectivity regions above the HRZs are caused by a decrease of reflection strength at layer interfaces or by destruction of laterally continuous layering for example, associated with deformation. Furthermore, we tested whether reflectivity reduction may be an artefact caused by limitations with seismic imaging of steeply dipping reflections.

We compared Lines P1, in which sediments above the BSR have normal reflectivity, and P3, in which a region of low reflectivity is present above the BSR. Both lines were collected with identical acquisition parameters (Table 1) and are therefore suitable for comparison. Figure 4 displays the portions of both lines as instantaneous-phase plots that facilitate tracing of weak reflections from layer interfaces. The low-reflectivity zone in Line P3 displays chaotic reflections in the instantaneous-phase plots making it unlikely that reflectivity reduction is caused by a decrease of impedance contrasts across laterally continuous layers. Some fragments of reflections are present with a dip that is significantly lower than that of the strong and continuous reflections in Line P1. It is therefore unlikely that the loss of reflectivity is an artefact from limitations with imaging steeply dipping reflections.

4. Interpretation

4.1 Nature of the High-Amplitude Events

The high-amplitude reflections start at BSRs and appear to disrupt BSRs along some of the lines. It is therefore likely that the HRZs are associated with gas hydrates and free gas rather than stratigraphic changes. Crutchley et al. (2006) came to the same conclusion for an HRZ along Line 05CM-38, which coincides with Line P6 (see Figure 1 for locations).

The images of high-amplitude reflections above BSRs at first sight look similar to gas-hydrate-bearing channel sands in the Nankai Trough (e.g., Saeki et al., 2008; Shimoda et al., 2008). Detection of hydrate-bearing sands off New Zealand would be important from a resource perspective. However, the pronounced seismic impedance decrease at a reflection segment along Line P4 (Section 3.3) is difficult to reconcile with the presence of gas hydrates, which would be predicted to lead to a seismic velocity increase and thus, positive-polarity reflection. We suggest the most likely explanation for a pronounced low-impedance layer is free gas in the sediment pore space. The only scenario we could envision for generating such a negative impedance contrast without the presence of free gas is a layer with a gradational increase of hydrate concentration with depth (not leading to any reflection) and a sharp contrast to gas-hydrate-free sediments at its base. Such a scenario has not been observed anywhere else, to our knowledge. Results from full-waveform inversion (Crutchley, 2009) show a pronounced low-velocity layer, typical of free gas, in the high-amplitude zone along Line 05CM-38. We conclude that the most likely cause for the HRZs is free gas above the regional level of BSRs. This interpretation does not rule out that gas hydrates are also present in the vicinity of gas layers and that they contribute to reflectivity.

We note that upon closer inspection of images published in the literature, there may be potentially significant differences between the Nankai Trough images and the data presented here. 3-D seismic data from the Nankai Trough appear to show mostly positive reflection coefficients at the top of the high-amplitude zones. Negative reflections seem to be largely confined to the edges of the high-amplitude zones where the top of high reflectivity is close to the BSR, unlike the negative-polarity reflector along Line P3 ~0.2 s above the regional level of the BSR.

On Line P9, a reflection band can be observed above the BSR level of the BSR. The upper-most reflection seems to have negative polarity with respect to the seafloor reflection (Figure 3) but amplitudes are relatively weak and the reflections appear to form folded, continuous layers. Our preliminary interpretation of these reflections therefore is that they mark stratigraphic boundaries but we cannot rule out free gas, perhaps at lower concentrations than along Lines P3-P6. Even if the reflection band in Line P9 was caused by free gas, our conclusions below regarding the presence of gas above regional BSR levels would not be affected significantly.

Because of the overall similarity to images from the Nankai Trough, we do not conclusively rule out the possibility that the high-amplitude reflections beneath the Porangahau Ridge are caused by gas-hydrate-bearing sands. However, our data analysis supports evidence for free gas above the regional level of BSRs.

4.2 Reflectivity Reduction in the Gas Hydrate Stability Zone

Gas hydrates may cause amplitude blanking (Lee et al., 1993). In a layered package of sediments with varying porosity, an even saturation of hydrate as a fraction of pore space results in preferential filling of high-porosity layers. Since seismic velocity decreases with porosity, preferential hydrate occurrence in high-porosity layers then leads to a stronger velocity increase compared to low-porosity layers. This causes a reduction of velocity contrasts and hence, reflection coefficients. Likewise, hydrate cementation, if it takes place, is intuitively thought to lead to a more uniform, that is, less reflective, sediment column. Gas-hydrate-related amplitude blanking (Lee et al., 1993) would cause a reduction of amplitudes at continuous layer interfaces. The instantaneous-frequency displays would be expected to show continuous arrivals in the blanked zones, which is not the case (Figure 4). We therefore conclude it is unlikely that the low reflectivity is caused by hydrate-related amplitude blanking.

Elevated attenuation of seismic waves in gas-hydrate-bearing sediments, as observed recently in sonic logs (Guerin and Goldberg, 2005; Matsuchima, 2006) may lead to a reduction of seismic amplitudes beneath hydrates. However, BSR strength appears to increase slightly between Lines P2 (without “blanking”) and P4 (with “blanking” above the BSR). Attenuation is therefore also unlikely to be the cause of amplitude reduction.

On the other hand, the loss of laterally coherent reflections within the low-reflectivity zones is compatible with small-scale folding and faulting. We therefore suggest that, while gas hydrates may play a role for some of the wide-spread blanking observed elsewhere on the margin (e.g., seismic profiles in Pecher and Henrys, 2003), in our study area, a destruction of horizontally continuous layer packages during deformation is the most likely cause for a reduction of reflectivity.

5. Discussion

5.1 Causes of Gas within the Regional Hydrate Stability Zone

The seismic data show evidence for free gas above the regional level of BSRs. This observation suggests that either gas is present within the hydrate stability field or that the BGHS is locally warped upwards.

Significant upwarping of the BGHS due to an increase in pore water salinity above salt diapirs as proposed for parts of the Gulf of Mexico (Ruppel et al., 2005; Coffin et al., 2008b) is unlikely in our study area because there is no evidence for salt diapirs along this margin. We will discuss two other possible causes: (1) invasion of free gas into the hydrate stability zone and (2) local upwarping of the BGHS due to expulsion of warm fluids.

Gas Invasion

Multiphase models of gas migration into the gas hydrate stability zone predict that free gas can move into and through the gas hydrate stability zone if hydrate formation is inhibited. Liu and Flemings (2007) predict that a salinity increase after salt exclusion from the clathrate structure is the most significant inhibitor for hydrate formation allowing gas and hydrate to co-exist in chimneys through which gas migrates to the seafloor.

Measurements with seafloor temperature probes that penetrated the seafloor down to ~3 m beneath the seafloor (mbsf), only show moderate thermal anomalies across the ridge (Pecher et al., 2007; Coffin et al., 2008a; Wood et al., 2008), although with evidence for fluid advection on the western side of the ridge (Schwalenberg et al., this issue). Invasion of free gas into the hydrate stability zone would be compatible with the absence of a pronounced thermal anomaly because the low heat capacity of gas (e.g., Liu and Flemings, 2007) makes advective heat transport inefficient. However gas invasion is unlikely for two reasons:

(1) The models of Liu and Flemings (2007) predict low gas saturation, generally below 2-3% even in the centre of gas chimneys, with coexisting hydrate at a saturation mostly above 50%. Using rock physics models, we predict the velocity increase from gas hydrate saturation to mostly offset the decrease from the addition of gas leading to a positive or only moderate negative reflection coefficient at the top of a region with coexisting gas and hydrate (Appendix A, Figure A.1), not the strong negative reflection coefficient observed in our data.

(2) Migration of free gas requires ample supply of gas from below. We interpret the fragmentation and partial disappearance of BSRs to the south in our study area as an indication that gas is being depleted. Gas supply therefore seems to be limited. No vent sites have been detected from echosounder and backscatter data, methane concentration in the water column is normal, and methane concentrations in piston cores are low (Pecher et al., 2007; Coffin et al., 2008a). Although it is possible that we have missed localized occurrences of vent sites, the above observations are indicative of relatively low supply rates of methane. We therefore conclude that, while we cannot rule out gas invasion, advective heatflow resulting in local

upwarping of the BGHS is a more likely explanation for the presence of gas above the regional level of BSRs.

Advective heatflow

Advective heatflow from expulsion of warm fluids may lead to local upwarping of the BGHS, similar to possible gas chimneys on the Cascadia margin (Wood et al., 2002). Depending on the mobility of gas compared to the speed at which the BGHS is moving upward, the upper termination of the HRZs would be located at or below the current local level of the BGHS: If gas migration can not "keep up" with an upward-moving BGHS, it is possible that the local level of the BGHS is above the top of the high-amplitude regions.

5.2 Thermal Gradient from the Depth of the High-Reflectivity Zones

The thermal gradient across the ridge was constrained assuming that the top of the high-reflectivity zones marks the local BGHS (Figure 5). Based on pore water chemistry in piston cores (Coffin et al., 2008a), we used pure methane hydrate in seawater (Dickens and Quinby-Hunt, 1994) to calculate the phase boundary with the *CSMHYD* software (Sloan, 1998). Bottom water temperatures were extracted from various CTD measurements in the past decades (Chiswell, 2000; Chiswell, 2002; Chiswell, 2005 and references therein, shown in Pecher et al., 2005). Since the short-streamer data did not allow velocity determination, we used an empirical depth / two-way traveltime (TWT) function (Townend, 1997a; Appendix B) to convert time sections to depth. We did not account for sedimentation rates which are considered low over anticlines along the margin (e.g., Lewis and Kohn, 1973), and we neglected heat refraction, since the surface topography is quite smooth.

The thermal gradient away from the high-amplitude zones is ~0.025 K/m. Where BSRs are present across the anticlines, there is an apparent long-wavelength increase of heatflow to almost 0.03 K/m. The high-amplitude reflections mark a sharp increase in thermal gradient to >0.05 K/m along lines P5 and P6.

We estimate the absolute error for thermal-gradient calculations to be ~35% with contributions of roughly 15% from velocity errors, and 10% each from sedimentation effects and the assumption of hydrostatic pressure (Appendix C). The apparent long-wavelength increase of the thermal gradient by ~0.005 K/m across the anticline in Lines P1 and P2 could thus be an artefact caused by velocity variations (higher velocity in older, more consolidated material beneath the anticline) and changes in sedimentation rates (higher rates in the depositional centres of the slope basins). The high-amplitude zones however, assuming they mark the local level of the BGHS, are outside the error margin and represent a pronounced thermal anomaly.

We cannot constrain the southward extent of this inferred thermal anomaly. The lack of high-amplitude reflections above the regional BGHS may indicate a termination of the advective-heatflow anomaly. Combined with the observed break in BSRs we suggest that alternatively, gas may have been depleted during rapid fluid and gas migration. In this case the local BGHS would not be marked by HRZs in the seismic sections.

The seafloor heatflow data are still being evaluated (Wood et al., 2008). Transient heatflow could explain the apparent discrepancy between the pronounced thermal anomaly derived from the BGHS and a moderate anomaly from seafloor heatflow measurements. The thermal signal from fluid expulsion at the BGHS may not yet have reached the seafloor or fluid expulsion may have shut down from north to south and cooling from the seafloor has not yet reached the level of the BSR. Further data analysis will be required to reconcile both observations.

Thermal gradients away from the HRZs are low compared to other convergent margins. However, they are similar to the average thermal gradient of 0.023 K/m compiled from bottom-hole temperatures in boreholes offshore Hawke's Bay ~150 km further north (Field et al., 1997). Also, BSRs in our study area are at similar depth levels as elsewhere on the margin (Townend, 1997a; Henrys et al., 2003). We therefore can rule out that the low thermal gradients are caused by localized processes such as thermal blanketing from high sedimentation rates in the slope basins adjacent to the Porangahau Ridge.

5.3 Estimates of Advection Rates

Coupled conductive and advective heatflow leads to concave-upwards temperature profiles. We used a 1-D analytical solution of the differential equation for simultaneous conductive and advective heat transport (Bredehoeft and Papadopulos, 1965) to estimate the fluid flux required for the observed upwarping of the BGHS (Appendix D). This modelling assumes one-dimensional, strictly vertical migration of fluids without lateral variations in flux rates, as well as constant porosity and thus, thermal conductivity. The solution requires fixed temperatures at two depth levels and then allows calculation of the temperature-depth profiles between those levels as a function of Darcy velocities, that is, rates of fluid flux through a surface (Darcy velocities do not constitute a direct measure of the speed at which the fluids travel through sediments. They are independent of sediment porosity). The seafloor was selected as upper depth level. The lower depth level *L* (Appendix D) is taken to be the depth at which advection starts contributing significantly to heatflow.

We assumed three levels for *L*. Fluids that originate from compaction in the accretionary prism may migrate in a dispersed way at low rates and they may not transport any significant heat compared to conductive heatflow. However, advective heatflow may be significant after focussing of fluid flow from funnelling at the base of the slope basins, which are thought to be filled mostly with fine-grained low-permeability sediments (Field et al., 1997), into the Porangahau Ridge. This case was simulated by assuming L = 1500 mbsf, a rough estimate for the thickness of the slope basin west of the ridge. Advective heatflow originating deep in the accretionary wedge or at the décollement is modelled with L = 5000 mbsf, the estimated depth of the décollement beneath the Porangahau Ridge (after interpretation in Barnes et al., this issue). This situation describes fluids that originate in the accretionary wedge and are being funnelled into thrust faults. Alternatively, fluids may be expelled from the underthrust sediments. Along the décollement, fluids migrate almost parallel to isotherms and are not predicted to contribute significantly to vertical heatflow. Advection will start affecting vertical heatflow where fluids migrate from the décollement through thrust faults towards the seafloor. We also modelled an intermediate depth of L=2500 mbsf mimicking funnelling of fluids within the accretionary wedge. The temperature at these depth levels was estimated using the thermal gradient from the depth of BSRs away from the amplitude anomalies, assuming purely conductive heatflow. Other input parameters are listed in Table 2.

Resulting temperature profiles in Figure 6 show that in order to cause the thermal anomaly inferred from upwarping of the BGHS, Darcy velocities of ~5, 11, and 22 mm/yr are required for advective heatflow originating at the depth level of the décollement, at mid-depths in the outer wedge, and beneath the slope basins, respectively. The reason why rates of advection to maintain a given temperature deviation decrease with increasing depth is that the deeper the origin of advective heatflow, the higher the temperature of the fluids.

Several input parameters were varied to constrain the possible effects from the simplifications behind our estimates. The longer 2-D migration paths for dipping faults was mimicked by assuming L = 10000 m but with the same temperature as predicted for the décollement. This change only leads to a slight increase of predicted Darcy velocities to ~5.5 mm/yr and we conclude the underestimate of the length of fluid migration paths by assuming a 1-D setting does not affect our conclusions.

The assumption of constant porosity does not distort results strongly because advective heatflow is governed by Darcy velocities, that is, the flux rates of fluids, which are independent of porosity. Porosity affects our predictions only indirectly through thermal conductivity. For a high constant porosity of 0.5 down to the décollement, Darcy velocities would be predicted to be ~4 mm/yr.

An decrease of porosity and hence, increase of thermal conductivity with depth as expected due to compaction, translates to a decrease of the temperature gradient and thus, lower temperatures at greater depths, assuming constant heatflow (Appendix E). The assumed constant porosity of 0.33 (Table 2) down to 5000 mbsf leads to a temperature at the depth of the décollement of 127 °C. Lower predicted temperatures of fluids at the décollement after assuming an increase of conductivity with depth would require higher rates of fluid expulsion in order to maintain a given temperature deviation at the BGHS. We mimic an increase of thermal conductivity K_b with depth by calculating heatflow using the thermal gradient from the depth of the BSR and a thermal conductivity assuming an average porosity of ϕ=0.5 as a typical value for shallow sediments above the BSR (e.g., ODP Sites 808, 1173, 1174, Nankai Trough, shown in Screaton et al., 2002). The temperature at the depth of L=5000 m, the depth of the décollement, was then calculated from that heatflow but using K_b based on an average ϕ=0.33 (Table 2). For this gradient, temperature at the décollement is 98 °C. For modelling the effect of advective heatflow, we assumed a constant ϕ=0.33. Predicted Darcy velocities to lead to the observed shoaling of BSRs increase slightly to ~7.5 mm/yr (Figure 6b). These tests show that our estimates of Darcy velocities are robust for comparison with rates of across-margin fluid expulsion.

5.4 Fluid Budget of Accretionary Wedge and Origin of Fluid-flow Focussing

Previous estimates of average fluid expulsion showed that at least ~20 m^3 of fluids are expelled from the accretionary prism annually per meter along-margin, most of it from sediment compaction with some additional contribution from the smectite-to-illite transition (Townend, 1997b, summarized by Sibson and Rowland, 2003). We update these calculations, which are based on the height of the sediment column above and below the décollement at the deformation front (Appendix F).

The total volume of water entering the system in both accreted and subducted sediments is estimated at ~53 m^3 yr^{-1} m^{-1} (i.e., per meter along margin) with an additional 3.8 m^3 yr^{-1} m^{-1} bound to smectite (see Appendix F). Under the assumption that only sediment above the décollement is incorporated into the accretionary wedge, the rate of fluids expelled from the accretionary wedge is ~39 m^3 yr^{-1} m^{-1} with an additional ~2.4 m^3 yr^{-1} m^{-1} from clay dehydration. Beneath the décollement, 11 m^3 yr^{-1} m^{-1} of water are assumed to enter the subduction zone plus an additional 1.4 m^3 yr^{-1} m^{-1} bound in smectite. These numbers are higher than the previous minimum estimates (Townend, 1997b) mainly because of greater thickness and higher assumed porosity of the incoming trenchfill section. We estimate our error to be less than 50% (Appendix F).

The seismic HRZ beneath the western part of the ridge in Lines P3-P6 stretches over roughly 500 m along margin-strike after correction for the ~15° angle between the large-scale margin strike and the local strike of the ridge, perpendicular to which the lines were acquired. Under the assumption that the HRZ marks the area of fluid expulsion, the above advection rates (Section 5.3) translate to 2.5 m^3 of fluids that are expelled per year for each meter along the margin for an origin of advective heatflow at the level of the décollement. Volumes for funnelling of fluid flow in the accretionary wedge and beneath the slope basins are 5.5 and 11 m^3 m^{-1} yr^{-1}, respectively.

An expulsion of 11 m^3 m^{-1} yr^{-1} is high compared to the estimated 39 m^3 yr^{-1} of the total fluid volume expelled from the accretionary wedge and the total volume of 57 m^3 m^{-1} yr^{-1} of fluids subducted and accreted on this margin, including clay-bound water: This would imply that almost 29% of dewatering of the accretionary wedge and >19% of the water entering the margin would be funnelled through Porangahau Ridge. The unknown width of the zone of fluid expulsion is probably the largest source of error for our volume estimates. Assuming somewhat arbitrarily, that the error in the width of the fluid-expulsion zone, and thus volumes, is on the order of 50% (width of 250-750 m), would still suggest that even for the lower end ~14% of dewatering of the accretionary prism would take place through a 250-m wide segment of the Porangahau Ridge, which is high considering that much of the compaction and thus, dewatering may take place seaward of the ridge.

We therefore suggest funnelling of fluids beneath low-permeability slope basins is unlikely to be the cause for the advective heat-flow anomaly. An origin of focussed fluid flow deeper within the accretionary wedge or at the décollement is volumetrically more conceivable. About 7% (*L*=5000 mbsf) to 14% (*L*=2500 mbsf) of fluid expulsion from the accretionary wedge is then predicted to take place through the Porangahau Ridge. An origin of advective heatflow from fluids that cross the décollement would require that ~20% of fluids that enter the subduction zone beneath the décollement (including clay-bound water) would be expelled through the ridge. While this number is relatively high, interpreted seismic sections show that the thrust fault beneath the Porangahau Ridge reaches the décollement (Barnes et al., this issue) and may thus act as fluid conduit. We therefore conclude that fluid focussing most likely takes place deep in the accretionary prism or at the décollement with fluids being sourced from the deep accretionary wedge and/or underthrust sediments. Our seismic data are not suited to shed light on how fluids migrate across the décollement into the thrust ridges. Suggested mechanisms include hydrofracturing (e.g., Vannucchi et al., 2008) and down-stepping of the décollement (e.g., Saffer et al., 2008).

Even though we do not predict funnelling of fluids beneath the slope basins to significantly disturb the thermal gradient, it may take place and may be an important mechanism controlling the distribution of BSRs and gas hydrates. BSRs on the Hikurangi margin are generally confined to structures that promote fluid flow, in particular thrust ridges (Pecher and Henrys, 2003; Henrys et al., in press), whereas they are usually absent in the slope basins. This observation suggests that in the thrust ridges, methane flux into the gas hydrates stability zone is sufficient to maintain

BSRs. Funnelling of gas-rich fluids into the ridges would be a feasible mechanism to locally increase methane flux into the hydrate stability zone.

5.5 BSR Gaps and Fluid Expulsion

The zone of fluid expulsion through the ridge may extend further south. We interpret the disappearance of the anomalies south of Line P6, combined with a decrease of BSR strength and continuity as well as the presence of a gap in BSRs at the position where the anomalies exist further north, as an indication that fluid expulsion also takes place further south, depleting the sediments of gas. NewVent Line S6 (Figure 7), which crosses the ridge ~10 km south of Line P9, displays features similar to the southern CHARMNZ lines: a weak BSR beneath the edges of the ridge and a BSR gap beneath its centre. This observation indicates that fluid expulsion may extend over 10 km along the margin. On the other hand, a more continuous BSR is present beneath the Porangahau Ridge in Line S3 (Figure 7), ~30 km north of Line P1. This suggests that the BSR is continuous across the ridge in the entire region between the CHARMNZ study area and S3. We caution that the structural setting may be different, with the ridge being interpreted by Barnes et al. (this issue) to be located above the seaward edge of the Cretaceous-Paleogene foundation.

BSRs across many other thrust ridges on this margin are continuous without displaying noticeable upwarping (Pecher and Henrys, 2003). Significant advective heat flow therefore does not seem to occur commonly beneath thrust ridges. However, at some other locations, gaps in BSRs can be observed beneath anticlines (e.g., Figure 8; see Figure 1 for location). With the CHARMNZ data, we may coincidently have mapped the northern edge of a region with focussed fluid expulsion and see indications of free gas “pulling away” from the BSR. We suggest that similar gaps in otherwise continuous BSRs beneath thrust ridges may mark locations of focussed fluid expulsion on the Hikurangi Margin.

5.6 Role of Structural Permeability

The reflectivity reduction above BSRs in the study area appears to coincide with destruction of sediment layering. We propose that fracturing during deformation leads to increased structural (or secondary) permeability beneath the Porangahau Ridge. The lateral extent of the inferred advective-heatflow anomalies suggests that, at the level of the BGHS, fluid flow is not limited to individual faults but is more diffuse over ~500 m. We advocate that, while deeper in the accretionary wedge, fluid flow may be highly focussed through thrust faults, it may become more diffuse close to the seafloor, facilitated by structural permeability. Indications for similar dispersion of fluid flow near the seafloor have been observed elsewhere e.g., on the Nankai accretionary margin (Henry et al., 2002), where diffuse fluid migration takes place through sediments in the hanging wall above thrust faults. On the Nankai margin, this was explained by higher intrinsic permeability of layer outcrops above the thrust.

For the last ~50-100 m beneath the seafloor along Line P6, fluids appear to take the "path of least resistance" to the seafloor through the edge of slope-basin sediments rather than the longer path to the location where the core of the anticline breaches the seafloor. Fluid flow through the edge of the slope basin is supported by a moderate advective signature of seafloor thermal gradients, "wiggliness" in the character of near-seafloor reflections, and a subsurface resistivity anomaly that is probably caused by gas hydrates (Schwalenberg et al., this issue). Along Line P4, near-seafloor fluid escape through what appear to be thin layers of a largely undeformed drape may be focussed through individual extensional faults. These faults may be dilated by overpressure from upward migrating fluids.

Figure 9 summarizes our model for fluid expulsion in the study area. Fluids originating in the subducted sediments and deep in the accretionary wedge migrate upwards along a thrust fault. Close to the seafloor, they may “fan out”, migrating into the hanging wall because of increased structural permeability, crossing the BGHS in a cross section of roughly 500 m and leading to a heatflow anomaly. A BSR gap develops due to a loss of gas in conjunction with fluid expulsion. Right beneath the seafloor along Line P6, we suggest fluids migrate along the edge of the slope basin taking the “path of least resistance” to the seafloor, leading to concave thermal gradients typical of advective heatflow (Schwalenberg et al., this issue). Along Line P4, extensional faults may facilitate focussed fluid expulsion to the seafloor.

6. Conclusions

We observe high-reflectivity zones beneath the Porangahau Ridge that originate at the regional level of BSRs and disrupt BSRs in the southern part of the study area. Based on negative polarity and high reflection strength, we interpret the HRZs as being primarily caused by free gas but do not entirely rule out alternative models. The most likely cause for gas above the regional level of BSRs is a pronounced thermal anomaly leading to local upwarping of the BGHS. Estimates of flux rates required to produce this thermal anomaly suggest that fluid-flow focussing originates in the deeper parts of the accretionary prism and the subducted sediment section. Zones of low reflectivity are present above the HRZs and appear to be linked to deformation of sediment layering rather than gas-hydrate-related amplitude blanking. We propose that fluid expulsion through the thrust ridge is facilitated by an increase of structural permeability by the formation of fractures during deformation.

7. Acknowledgments

We would like to thank captains and crews of *R/V Tangaroa* voyage TAN0607 and *R/V Sonne* SO191 for excellent seamanship. We would also like to thank Nathan Bangs and an anonymous reviewer for their constructive comments and Keith Lewis as guest editor for handling of this manuscript. TAN0607 on the Porangahau Ridge was funded by the New Zealand Foundation of Research, Science, and Technology (FRST, contract C05X0302 to GNS Science), GNS and NIWA Capability Funds, NRL research focus on an Advanced Research Initiative (ARI "Quantify the processes responsible for the distribution of gas hydrate (meters to hundreds of meters scale) associated with representative seafloor seeps"), the Office of Naval Research and Office of Naval Research-Global sponsored program for the Marine Biogeochemistry Section (Naval Research Laboratory and Hawaii Natural Energy Institute, University of Hawaii for International Collaboration on Methane Hydrate Research and Development), and the Department of Energy (National Energy Technology Laboratory National Methane Hydrate R & D). SO191 was funded by the German Federal Ministry of Education and Research (BMBF), grant no. 03G0191A.

Appendix A – Rock Physics Modelling of Reflection Coefficients

We estimated the gas saturation required to generate the strong reflection with negative polarity from the top of the high-amplitude zone along Line P3 (Figure 3a). Liu and Flemings (2007), in most models typically predict only 2-3% of gas to be present within the gas hydrate stability zone coexisting with 20-80% of gas hydrates in the pore space – a conceptual gas chimney typical for their models is shown in Figure A.1a. We will show that these low saturations of gas coexisting with high gas hydrate saturations are unlikely to cause such a negative-polarity reflection. For calibration of reflection coefficients, the average seafloor reflection coefficient between 4.81 and 6.06 km was calculated as 0.23(±0.04) by comparing amplitudes of the seafloor reflection and the water-bottom multiple. After correction for geometrical spreading, but not attenuation and transmission losses from reflections, the reflection coefficient from the top of the high-amplitude anomaly is approximately -0.25 (correction for attenuation and other transmission losses would increase the absolute value slightly).

We first estimated the reflection coefficient from gas in the pore space in the absence of gas hydrate for both even (Domenico, 1977) and “patchy” distributions (Dvorkin et al., 1999). In the case of “patchy” gas distribution, some regions of the sediment are thought to be fully gas saturated while others are fully water saturated on mesoscopic scales (larger than pore sizes but significantly smaller than seismic wavelengths). Target depth was ~3.2 s TWT, i.e., 0.52 s beneath the seafloor, equivalent to 474 mbsf using a regional TWT-depth function (Townend, 1997a; Appendix B). This is the level of the coherent reflection used for investigating wavelet polarities (see Figure 3). We estimated background velocity of gas- (and hydrate-) free sediments from the same TWT-depth function. Porosity was also estimated from this velocity (Hamilton, 1978). Gas-free sediments were modelled as packed spheres (Mindlin, 1949; Hashin and Shtrikman, 1963) as outlined by Helgerud et al. (1999), assuming hydrostatic pressure in the pore space. We added clay to the sediment matrix to lower velocities (Table A.1) in order to match our velocity-TWT function. Errors from this arbitrary approach for defining a deterministic model are largely alleviated by focussing on the impedance contrasts that cause reflections, rather than absolute velocities. For calculating reflection coefficients, the decrease of density from a replacement of pore water by gas was taken into account. Input parameters are listed in Table A1. Gas saturation for a reflection coefficient of -0.25 is predicted to be between 7% and 70% for even and “patchy” distribution, respectively (Figure A.1b), i.e., even without any co-existing hydrate and assuming evenly distributed gas, the predicted saturation of 2-3% from gas invasion is not sufficient to cause the observed reflection coefficients.

Gas hydrate was added using the same deterministic rock physics models (Helgerud et al., 1999). In these models, gas hydrate has three principal modes of distribution, disseminated (“floating”) in the pore space without any grain contact, part of the load-bearing frame (matrix), and grain-contact or grain-coating cement (Helgerud et al., 1999; Ecker et al., 2000). Laboratory studies and geometric considerations (e.g., Yun et al., 2007) suggest that in sands, gas hydrates at a saturation above ~40% exercise grain contact and hence, a dissemination model is not appropriate at the concentrations investigated here. We therefore assumed a matrix model by adding hydrate “grains” to the matrix using the Hill average (Hill, 1952; Helgerud et al., 1999). A reflection coefficient of -0.25 is not reached even for the most extreme case, 40% gas hydrate saturation, 60% gas saturation. For the majority of their models, with 50-80% of gas hydrate saturation, we would even predict a slightly positive reflection coefficient at the top of the chimneys. While other scenarios could be construed in which negative reflection coefficients will be achieved (e.g., coexisting gas and hydrate beneath a thick gas-free layer with high gas hydrate saturation and with a gradational top that does not generate a reflection), our conceptual models suggest that the low gas saturations predicted from modelling (Liu and Flemings, 2006; Liu and Flemings, 2007) make it unlikely that gas invasion leads to a negative reflection coefficient of -0.25.

Appendix B – TWT-Depth Function

For depth conversion and velocity profiles, we used an empirical TWT-depth function for this margin (Townend, 1997a):

$$\begin{aligned} &z = 82t^2 + 868t,\ \text{where} \\ &t = \text{TWT (s beneath the seafloor)} \\ &z = \text{depth (mbsf)} \end{aligned}$$

We used this empirical function because the short-streamer data shown here do not allow velocity analysis. Velocity analysis along Line 05CM-38 is still in progress and would only be applicable directly to Line P6. The error of using this TWT-depth function was estimated by comparing it to results from velocity analyses at three locations along Line 05CM-38 where waveform inversion was conducted (Crutchley, 2009). Figure B.2 shows that the error for depth beneath the seafloor is <15%.

Appendix C – Error Estimates for Thermal Gradient

We identified four main sources of errors for the calculation of the thermal gradient, the effect of sedimentation, lateral velocity changes, deviation from hydrostatic pressure, and errors in the phase boundary from the assumption that methane is the only hydrate-forming gas. Townend (1997a), using typical sedimentation rates for this margin, calculated that sedimentation decreases the thermal gradient to the BGHS by about 10%. The error from resulting from velocity errors is <15% (Appendix B). Converting the TWT-depth function in Appendix B to velocities and using an empirical velocity-density relationship (Hamilton, 1978), lithostatic pressure at the BGHS away from the high-amplitude anomalies is predicted to be ~6.2 MPa higher than hydrostatic pressure, translating to an increase of the temperature at the phase boundary by ~2.0 K and an increase of the thermal gradient by ~0.0026 K/m, i.e. ~10% (Figure C.1). Using a natural-gas mix based on onshore vents, excluding Structure-II forming propane (Giggenbach et al., 1993b, in Pecher et al., 2005), only has a negligible effect on the thermal gradient (Figure C.1). Combined, we estimate the absolute error of the thermal gradients to be <35%, noting that the error in relative changes across the heatflow anomalies is likely to be considerably less.

Appendix D – Estimate of Fluid Advection

We estimate the rate of fluid advection based on a common approach summarized by Land and Paull (2001) and Arriaga and Leap (2006). The equation for simultaneous transfer of heat and water assuming simultaneous, 1-D heatflow, incompressible fluids, in a homogenous, isotropic, fully saturated medium (e.g., Stallman, 1963) is given by:

$$\rho_b C_b \frac{\partial T}{\partial t} = K_b \frac{\partial^2 T}{\partial z^2} - \rho_f C_f v_d \frac{\partial T}{\partial z}, \text{ where}$$

ρ : density
C : specific heat capacity
T : temperature
t : time
K : thermal conductivity
z : depth
v_d : Darcy (or filtration) velocity
Indices: f : fluid, b : bulk sediment

For steady-state conditions, i.e., no changes with time, this equation is simplified to:

$$K_b \frac{\partial^2 T}{\partial z^2} = \rho_f C_f v_d \frac{\partial T}{\partial z}$$

We here use the analytical solution to this equation for temperature with depth *T(z)* (Bredehoeft and Papadopulos, 1965):

$$\frac{T(z) - T(0)}{T(L) - T(0)} = \frac{e^{\beta z/L} - 1}{e^{\beta} - 1}, \text{ where } \beta = \frac{C_f \rho_f v_d L}{K_b}$$

T(0) and *T(L)* are known temperatures at the seafloor and depth *L* beneath the seafloor. This solution yields the concave profile typical of heatflow measurements in the presence of advection. In our case, *T(L)* is the temperature at which we assume focussed fluid flow to originate. We then vary v_d to match temperatures at the BGHS. Bulk thermal conductivity is calculated using the geometric mean between pore water and grain material (e.g., Villinger et al., 1994) as

$$K_b = K_f^{\phi} K_g^{(1-\phi)}, \text{ where}$$

ϕ : porosity,
index g : grain

Appendix E – Increase of Thermal Conductivity with Depth

The 1-D equation for conductive, steady state heatflow, with sign convention and notations similar to Townend (1997a) is:

$$q = K_b \frac{dT}{dz}, \text{ where}$$

K_b : thermal conductivity

$\frac{dT}{dz}$: thermal gradient

(a minus sign is sometimes introduced to account for the fact that heat is flowing from hotter to cooler, i.e., deeper to shallower depths; Fowler, 1990). We assume constant heatflow with depth down to the décollement, i.e., an absence of heat sources in the accretionary prism. K_b is expected to increase with depth because of a decrease of porosity resulting in a decrease of dT/dz with depth. Linear extrapolation of temperatures using dT/dz from the depth of BSRs then leads to an overestimate of temperatures at greater depths.

Appendix F – Rates of Fluid Input and Expulsion

We adjusted first estimates of the fluid budget of the Hikurangi Margin's accretionary prism (Townend, 1997b) to our study area. Using the simplification that only sediments above the décollement are accreted and that fluid influx from the subducted sediment across the décollement into the accretionary prism is not significant for the fluid budget of the prism, the volume of pore water that is accreted into the accretionary prism per time and per meter along the margin (V_{accr}) can be calculated from the thickness of the trenchfill material above the décollement seaward of the deformation front as:

$$V_{accr} = v h_{accr} \phi_{accr}$$

where v is the subduction velocity, h_{accr} the thickness of the incoming trenchfill material above the décollement, and ϕ_{accr} the porosity above the décollement. The volume of water released during compaction of the accretionary prism (V_{comp}) is

$$V_{comp} = \frac{v h_{accr} \left(\phi_{accr} - \phi_{comp} \right)}{1 - \phi_{comp}}$$

where ϕ_{comp} is the porosity of sediments accreted into the accretionary prism. The volume of clay-bound water released in the deep accretionary prism from smectite dehydration (V_{hydac}) is

$$V_{hydac} = SWv h_{accr} \left(1 - \phi_{accr} \right)$$

where S is the volumetric fraction of smectite in the sediments and W the volumetric fraction of water in smectite. We also constrained the total amount of water entering the subduction system by adding the volume of pore and clay-bound water in the subducting sediments (V_{sub} and V_{hydsub}, respectively) as:

$$V_{sub} = v h_{sub} \phi_{sub}$$

$$V_{hydsub} = SWv h_{sub} \left(1 - \phi_{sub} \right)$$

where, h_{sub} and ϕ_{sub} are thickness and porosity, respectively, of the incoming trenchfill material below the décollement. Input parameters and results, compared to Townend (1997b) are listed in Table E.1. We roughly estimate the errors in our volume constraints as <50% (20% velocity-related, 20% porosity-related, 10% from other input parameters).

References

Arriaga, M.A., Leap, D.I., 2006. Using solver to determine vertical groundwater velocities by temperature variations, Purdue University, Indiana, USA. Hydrogeol. J., 14, 253-263.

Ballance, P.F., 1976. Evolution of the Upper Cenozoic magmatic arc and plate boundary in northern New Zealand. Earth Planet. Sci. Lett., 28, 356-370.

Barnes, P.M., Mercier de Lepinay, B., 1997. Rates and mechanics of rapid frontal acrretion along the very obliquely converget southern Hikurangi margin, New Zealand. J. Geophys. Res., 102, 24931-24952.

Barnes, P.M., Mercier de Lepinay, B., Collot, J.-Y., Delteil, J., Audru, J.-C., 1998. Strain partitioning in the transition area between oblique subduction and continental collision, Hikurangi margin, New Zealand. Tectonics, 17, 534-557.

Barnes, P.M., Lamarche, G., Bialas, J., Henrys, S.A., Pecher , I.A., Netzeband, G., Greinert, J., Mountjoy, J.J., Pedley, K., Crutchley, G., this issue. Tectonic and Geological Framework for Gas Hydrates and Cold Seeps on the Hikurangi Subduction Margin, New Zealand. Mar. Geol.

Beanland, S., 1992. The North Island dextral fault belt, Hikurangi subduction margin, New Zealand, PhD thesis, Victoria University of Wellington.

Bialas, J., Greinert, J., Linke, P., Pfannkuche, O. (Editors), 2007. FS Sonne Fahrtbericht / Cruise Report SO 191 New Vents, 9. IFM-GEOMAR, Kiel, 186 pp.

Bohrmann, G., Heeschen, K., Jung, C., Weinrebe, W., Baranov, B., Cauilleau, B., Heath, R., Hühnerbach, V., Hort, M., Masson, D., Trummer, I., 2002. Widespread fluid expulsion along the seafloor of the Costa Rica convergent margin. Terra Nova, 14, 69-79.

Bredehoeft, J.D., Papadopulos, I.S., 1965. Rates of vertical groundwater movement estimated from the earth's thermal profile. Water Resour. Res., 1, 325-328.

Chiswell, S., 2000. The Wairarapa Coastal Current. N. Z. J. Mar. Freshw. Res., 34, 303-315.

Chiswell, S., 2002. Wairarapa Coastal Current influence on sea surface temperature in Hawke's Bay, New Zealand. N. Z. J. Mar. Freshw. Res., 36, 267-279.

Chiswell, S., 2005. Mean and variability in the Wairarapa and Hikurangi Eddies. N. Z. J. Mar. Freshw. Res., 39, 121-134.

Coffin, R., Hamdan, L., Pohlman, J., Wood, W., Pecher, I., Henrys, S., Greinert, J., Faure, K., Gorman, A., Orpin, A., 2008a. Geochemical Characterization of Concentrated Gas Hydrate Deposits of the Hikurangi Margin, New Zealand. NRL-6110-2007, U.S. Naval Research Laboratory.

Coffin, R.B., Hamdan, L., Plummer, R., Smith, J., Gardner, J., Wood, W.T., 2008b. Analysis of methane and sulfate flux in methane-charged sediments from the Mississippi Canyon, Gulf of Mexico. Mar. Petrol. Geol., 25, 977-987.

Crutchley, G.J., Pecher , I.A., Henrys, S.A., Gorman, A.R., 2006. Gas hydrate "sweet spots" on the Hikurangi margin, from recently acquired multi-channel seismic data, Proc. New Zealand Petrol. Conf., Auckland, 7pp.

Crutchley, G., 2009. Gas hydrates on New Zealand's Hikurangi Margin: the importance of focused fluid flow for highly-concentrated deposits, methane seepage, and seafloor erosion, PhD thesis, University of Otago, Dunedin.

DeMets, C., Gordon, R.G., Argus, D.F., Stein, S., 1994. Effect of recent revisions to the geomagnetic reversal time scale on estimates of current plate motions. Geophys. Res. Lett., 21, 2191-2194.

Dickens, G.R., Quinby-Hunt, M.S., 1994. Methane hydrate stability in seawater. Geophys. Res. Lett., 21, 2115-2118.

Domenico, S.N., 1977. Elastic properties of unconsolidated porous sand reservoirs. Geophysics, 42, 1339-1368.

Dvorkin, J., Moos, D., Packwood, J.L., Nur, A., 1999. Identifying patchy saturation from well logs. Geophysics, 64, 1756-1759.

Ecker, C., Nur, A., Dvorkin, J., 2000. Estimating the amount of gas hydrate and free gas from marine seismic data. Geophysics, 65, 565-573.

Faure, K., Greinert, J., Pecher, I.A., Graham, I.J., Massoth, G.J., de Ronde, C.E.J., Wright, I.C., Baker, E.T., Olson, E.J., 2006. Methane seepage and its relation to slumping and gas hydrate at the Hikurangi margin, New Zealand. N. Z. J. Geol. Geophys., 49, 503-516.

Field, B.D., Uruski, C.I., Beu, A., Browne, G., Crampton, J., Funnell, R., Killops, S., Laird, M., Mazengarb, C., Morgans, H., Rait, G., Smale, D., Strong, P., 1997. Cretaceous-Cenozoic geology and petroleum systems of the east coast region, New Zealand. Institue of Geological and Nuclear Sciences Monograph, 19, Lower Hutt, New Zealand, 301 pp.

Fowler, C.M.R., 1990. The solid earth. Cambridge University Press, Cambridge, U.K., 472 pp.

Giggenbach, W.F., Sano, Y., Wakita, H., 1993a. Isotopic composition of helium, CO2 and CH4 contents in gases produced along the New Zealand part of a convergent plate boundary. Geochim. Cosmochim. Acta, 57, 3427-3455.

Giggenbach, W.F., Stewart, M.K., Sano, Y., Goguel, R.L., Lyon, G.L., 1993b. Isotopic and chemical composition of the waters and gases from the East Coast accretionary prism, New Zealand, Proc. Final Research Coordination Meeting on the Application of Isotope and Geochemical Techniques to Geothermal Exploration in the Middle East, Asia, the Pacific, and Africa, Dumaguete, Philippines, pp. 208-231.

Ginsburg, G.D., Soloviev, V.A., 1997. Methane migration within submarine gas hydrate stability zone under deep-water conditions. Mar. Geol., 137, 49-57.

Gray, D.E. (Editor), 1972. American Institute of Physics Handbook. McGraw-Hill, New York.

Guerin, G., Goldberg, D., 2005. Modeling of acoustic wave dissipation in gas hydrate–bearing sediments. Geochem., Geophys., Geosys., 6, 1-16.

Haeckel, M., Suess, E., Wallmann, K., Rickert, D., 2004. Rising methane gas bubbles form massive hydrate layers at the seafloor. Geochim. Cosmochim. Acta, 68, 4333-4345.

Hamilton, E.L., 1978. Sound velocity-density relations in sea-floor sediments and rocks. J. Acoust. Soc. Am., 43, 366-377.

Hashin, Z., Shtrikman, S., 1963. A variational approach to the elastic behavior of multiphase materials. J. Mech. Phys. Solids, 11, 127-140.

Helgerud, M.B., Dvorkin, J., Nur, A., Sakai, A., Collett, T., 1999. Elastic-wave velocity in marine sediments with gas hydrates: effective medium modeling. Geophys. Res. Lett., 26, 2021-2024.

Henry, P., Lallemant, S., Nakamura, K., Tsunogai, S., Mazzotti, S., Kobayashi, K., 2002. Surface expression of fluid venting at the toe of the Nankai wedge and implications for flow paths. Mar. Geol., 187, 119-143.

Henrys, S.A., Ellis, S., Uruski, C., 2003. Conductive heat flow variations from bottom-simulating reflectors on the Hikurangi margin, New Zealand. Geophys. Res. Lett., 30, 1065.

Henrys, S.A., Reyners, M., Pecher , I.A., Bannister, S., Nishimura, Y., Maslen, G., 2006. Kinking of the subducting slab by escalator normal faulting beneath the North Island of New Zealand. Geology, 34, 777-780.

Henrys, S.A., Woodward, D.J., Pecher , I.A., in press. Variation of bottom-simulating reflection (BSR) strength in a high-flux methane province, Hikurangi margin, New Zealand, AAPG Special Publication, pp. (accepted).

Hill, R., 1952. The elastic behavior of crystalline aggregate. Proc. Phys. Soc. London, A65, 349-354.

Katz, H.R., 1981. Probable gas hydrate in continental slope east of the North Island, New Zealand. J. Petrol. Geol., 3, 315-324.

Kukowski, N., Pecher, I.A., 1999. Thermo-hydraulic modelling of the accretionary complex off Peru at 12°S. J. Geodyn., 27, 373-402.

Land, L.A., Paull, C.K., 2001. Thermal gradients as a tool for estimating groundwater advective rates in a coastal estuary: White Oak River, North Carolina. J. Hydrol., 248, 198-225.

Lee, M.W., Hutchinson, D.R., Dillon, W.P., Agena, W.F., Swift, B.A., 1993. Method of estimating the amount of in situ gas hydrates in deep marine sediments. Mar. and Petrol. Geol., 10, 493-506.

Lewis, K.B., Kohn, B.P., 1973. Ashes, turbidites and rates of sedimentation on the continental slope off Hawkes Bay. N. Z. J. Geol. Geophys., 16, 439-454.

Lewis, K.B., Pettinga, J.R., 1993. The emerging imbricate frontal wedge of the Hikurangi margin, in: P.F. Balance (Ed.), South Pacific sedimentary basins. Sedimentary basins of the world 2, basins of the southwest Pacific. Elsevier, Amsterdam, pp. 225-250.

Lewis, K.B., Marshall, B.A., 1996. Seep faunas and other indicators of methane-rich dewatering on New Zealand convergent margins. N. Z. J. Geol. Geophys., 39, 181-200.

Liu, X., Flemings, P.B., 2006. Passing gas through the hydrate stability zone at southern Hydrate Ridge, offshore Oregon. Earth Planet. Sci. Lett., 241, 211-226.

Liu, X., Flemings, P.B., 2007. Dynamic multiphase flow model of hydrate formation in marine sediments. J. Geophys. Res., 112, B03101.

Mann, D., Kukowski, N., 1999. Numerical modelling of focussed fluid flow in the Cascadia accretionary wedge. J. Geodyn., 27, 359-372.

Matsuchima, J., 2006. Seismic wave attenuation in methane hydrate-bearing sediments: Vertical seismic profiling data from the Nankai Trough exploratory well, offshore Tokai, central Japan. J. Gephys. Res., 111, 1-20.

Mavko, G., Mukerji, T., Dvorkin, J., 1998. The Rock Physics Handbook. Cambridge University Press, Cambridge, U.K., 329 pp.

Mindlin, R.D., 1949. Compliance of elastic bodies in contact. Trans. SDME, 71, 259-268.

Minshull, T.A., White, R., 1989. Sediment composition and fluid migration in the Makran accretionary prism. J. Geophys. Res., 94, 7387-7402.

Moore, J.C., Vrolijk, P., 1992. Fluids in accretionary prisms. Rev. Geophys., 30, 113-135.

Pecher, I.A., Henrys, S.A., 2003. Potential gas reserves in gas hydrate sweet spots on the Hikurangi Margin, New Zealand. Science Report 2003/23, Institute of Geological and Nuclear Sciences, Lower Hutt.

Pecher, I.A., Henrys, S.A., Ellis, S., Chiswell, S.M., Kukowski, N., 2005. Erosion of the seafloor at the top of the gas hydrate stability zone on the Hikurangi Margin, New Zealand. Geophys. Res. Lett., 32, L24603.

Pecher, I.A., Coffin, R., Henrys, S.A., CHARMNZ Working Group, 2007. Cruise Report: gas hydrate exploration on the East Coast, North Island, New Zealand. Science Report 2007/29, GNS Science, Lower Hutt, New Zealand.

Ruppel, C., Kinoshita, M., 2000. Heat, methane, and energy flux in an active margin gas hydrate province, offshore Costa Rica. Earth Planet. Sci. Lett., 179, 153-165.

Ruppel, C., Dickens, G.R., Castellini, D.G., Gilhooly, W., Lizarralde, D., 2005. Heat and salt inhibition of gas hydrate formation in the northern Gulf of Mexico. Geophys. Res. Lett., 32, L04605.

Saeki, T., Fujii, T., Inamori, T., Kobayashi, T., Hayashi, M., Nagakubo, S., Takano, O., 2008. Delineation of methane hydrate concentrated zone using 3D seismic data in the eastern Nankai Trough, Proc. 6th International Conference on Gas Hydrates, Vancouver, 9 pp.

Saffer, D.M., Screaton, E.J., 2003. Fluid flow at the toe of convergent margins: interpretation of sharp pore-water geochemical gradients. Earth Planet. Sci. Lett., 213, 261-270.

Saffer, D.M., Underwood, M.B., McKiernan, A.W., 2008. Evaluation of factors controlling smectite transformation and fluid production in subduction zones: Application to the Nankai Trough. Island Arc, 17, 208-230.

Schwalenberg, K., Wood, W.T., Pecher , I.A., Hamdan, L.J., Henrys, S.A., Jegen, M.D., Coffin, R.B., this issue. Preliminary Interpretation of Electromagnetic, Heat Flow, Seismic, and Geochemical Data for Gas Hydrate Distribution Across the Porangahau Ridge, New Zealand. Mar. Geol.

Screaton, E., Saffer, D., Henry, P., Hunze, S., Leg 190 Scientific Party, 2002. Porosity loss within the underthrust sediments of the Nankai accretionary complex: Implications for overpressures. Geology, 30, 19-22.

Shimoda, N., Saeki, T., Inamori, T., Kobayashi, T., Fujii, T., 2008. Study results of picking high amplitude reflectors in turbidite channel to reveal detail of methane hydrate concentrated zone, Proc. 6th International Conference on Gas Hydrates, Vancouver, 4 pp.

Sibson, R.H., Rowland, J.V., 2003. Stress, fluid pressure and structural permeability in seismogenic crust, North Island, New Zealand. Geophys. J. Int., 154, 584-594.

Sloan, E.D., 1998. Clathrate hydrates of natural gases. Marcel Bekker, New York, 641 pp.

Stallman, R.W., 1963. Computation of ground-water velocity from temperature data. USGS Water Supply Paper 1544-H, 36-47.

Townend, J., 1997a. Estimates of conductive heat flow through bottom-simulating reflectors on the Hikurangi margin and southwest Fiordland, New Zealand. Mar. Geol., 141, 209-220.

Townend, J., 1997b. Subducting a sponge: minimum estimates of the fluid budget of the Hikurangi Margin accretionary prism. Geol. Soc. N.Z. Newsletter, 112, 14-16.

Vannucchi, P., Remitti, F., Bettelli, G., 2008. Geological record of fluid flow and seismogenesis along an erosive subducting plate boundary. Nature, 451, 699-703.

Villinger, H.W., Langseth, M.G., Göschel-Becker, H.M., Fisher, A.T., 1994. Estimating in-situ thermal conductivity from log data, in: M.J. Moul, E.E. Davis, A.T. Fisher, J.F. Slack (Eds.), Proc. ODP, Sci. Results. Ocean Drilling Program, College Station, TX, pp. 545-552.

Waite, W.F., Helgerud, M.B., Nur, A., Pinkston, J., Stern, L.A., Kirby, S.H., Durham, W.B., 1998. First measurements of P- and S-wave speed on pure methane gas hydrate, Suppl. to Eos, 10 Nov. 1998, AGU Fall Meeting, pp. 463.

Wang, K., Hu, Y., 2006. Accretionary prisms in subduction earthquake cycles: The theory of dynamic Coulomb wedge. J. Geophys. Res., 111, B06410.

Wood, W.T., Gettrust, J.F., Chapman, N.R., Spence, G.D., Hyndman, R.D., 2002. Decreased stability of methane hydrates in marine sediments owing to phase-boundary roughness. Nature, 420, 656-660.

Wood, W.T., Pecher, I., Henrys, S., Coffin, R., 2008. The transient nature of heat and fluid flux on the Porangahau Ridge, New Zealand, Eos Trans. AGU, Fall Meeting Suppl.

Xu, W., Ruppel, C.D., 1999. Predicting the occurrence, distribution, and evolution of methane gas hydrate in porous marine sediments. J. Geophys. Res., 104, 5081-5095.

Xu, W., 2004. Modeling dynamic marine gas hydrate systems. Amer. Miner., 89, 1271-1279.

Yamano, M., Uyeda, S., Aoki, Y., Shipley, T.H., 1982. Estimates of heat flow derived from gas hydrates. Geology, 10, 339-343.

Yun, T.S., Santamarina, J.C., Ruppel, C., 2007. Mechanical properties of sand, silt, and clay containing tetrahydrofuran hydrate. J. Geophys. Res., 112, B04106.

Zatsepina, Y., Buffett, B.A., 1997. Phase equilibrium of gas hydrate: Implications for the formation of hydrate in the deep sea-floor. Geophys. Res. Lett., 24, 1567-1570.

Figure Legends

Figure 1: Location maps.

Upper left: Margin east of North Island, New Zealand where the Pacific Plate (PAC) is subducted obliquely beneath the Australian Plate (AUS). Subduction rates and angle after DeMets et al. (1994), Henrys et al. (2006).

Lower left: Porangahau Ridge on lower slope with bathymetric contours at 500 m intervals with seismic tracks shown as black lines. Thick white lines mark seismic sections shown in the manuscript. P1-P9: Porangahau Ridge transects during CHARMNZ, *R/V Tangaroa* voyage TAN0607. S3 and S6: transects during NewVents, *R/V Sonne* voyage SO191, shown in Figures 7 and 8. 38: Industry-style line 05CM-38 (not shown here). Dashed white line marks the sub-surface position of the boundary between the pre-subduction Cretaceous-Paleogene Foundation (CPF) and Plio- to Pleistocene accreted trench-fill turbidites (PPT) of the outer wedge, after Barnes et al. (this issue).

Right: Detailed bathymetry with contours at 200 m intervals showing position of seismic lines P1 to P9. Dashed line marks 0 km in Figure 2.

Figure 2: Seismic transects, north to south. See Figure 1 for locations. Lines are 1.85 km apart. Amplitudes are corrected for geometric spreading and calibrated to the reflection coefficient of the seafloor in the slope basins (see Section 3.2). We focus on the north-to-south progression of the high-amplitude zone at 5-6 km.

Figure 3: Waveforms of seafloor reflections and reflections of interest after flattening of arrivals (i.e., aligning arrivals horizontally), see Figure 2 for locations.

A: Top of high-amplitude anomaly in Line P4, displayed with same amplitude scaling as seafloor reflection, after correction for geometric spreading.
B: Top of reflection band beneath anticline in Line P9, displayed after scaling amplitude by a factor of 2 compared to the seafloor. The "sharper" waveform, translating to higher frequencies, compared to Line P4 is caused by towing the streamer at shallower depth (Table 1). Waveforms from the seafloor and the top of the reflections are trough-peak-trough and peak-trough-peak sequences, respectively, suggesting a negative impedance contrast and thus a drop of velocity and/or density. The top of the high-amplitude anomaly in Line P4 generates a similarly strong arrival as the seafloor. Its reflection coefficient was calculated as -0.25 (Appendix A). The arrival from the top of the reflectivity band in Line P9 is less than half as strong as the seafloor reflection.

Figure 4: Standard seismic sections (left) and instantaneous-phase sections (right) across region of low reflectivity in Line P3 compared to Line P1, where reflectivity is normal. The zone of low reflectivity in Line P3 coincides with a chaotic region in the instantaneous-phase section. Fragments of reflections are present in the low-reflectivity region with a lower dip than some strong and continuous arrivals in Line P1.

Figure 5: Thermal gradient from the depth of BSRs and the top of the high-amplitude zones, assuming that they mark the local BGHS.

Figure 6: A: Predicted temperature profiles from advective heatflow with L=1500, 2500, and 5000 m (Appendix D). Labels are Darcy-velocities v_d in mm/yr. The

thermal gradient for conductive heatflow (v_d=0) is obtained from the depth of the BSR away from the anomalies. *L* describes the depth at which fluid advection starts contributing to heatflow. Left: *L*=1500 m (beneath the seafloor) mimics focussing of fluid flow beneath the slope basins. v_d=22 mm/yr is required to shift the BGHS from the level of the undisturbed BSR to the top of the high-amplitude zones. Centre: *L*=2500 as intermediate depth, predicting v_d=11 mm/yr, represents fluid focussing in the accretionary prism. Right: *L*=5000 m is roughly the depth of the décollement and describes focussed fluid expulsion from base of the accretionary wedge and from the underthrust sediments, predicting v_d=5 mm/yr.

B: Sensitivity of results to changes of input parameters, assuming advective heatflow originates at 5000 m. Left: A longer travel path (*L*=10000 m) with identical input parameters to those in right-most panel above otherwise, mimicking a dipping thrust fault, showing slight increase of v_d from 5 to ~5.5 mm/yr. Centre: Significantly higher porosity ϕ would cause a decrease of v_d to 4 mm/yr. Right: A decrease of ϕ with depth, simulated by using ϕ=0.5 for predicting heatflow from the depth of the BSR, but ϕ=0.33 for calculating temperatures at 5000 mbsf and for advection modelling, leads to an increase of predicted v_d to ~7.5 mm/yr. See Section 5.3 for further details.

Figure 7: Seismic lines across the Porangahau Ridge north (S3) and south (S6) of the study area respectively (locations in Figure 1 lower left), after (Barnes et al., this issue), re-processed using parameters similar to those for the data shown in Figure 2. Line S3 shows a mostly continuous BSR across the ridge although distinct amplitude anomalies appear to be present close to the seafloor. Line S6 has a clear break in the BSR, similar to the southern-most lines in our study area.

Figure 8: Seismic line S6 across a ridge seaward of Porangahau Ridge, re-processed as above (see Figure 1 for location). A clear break in the BSR is present. We speculate that BSR gaps indicate depletion of gas from fluid expulsion and, if so, are a signature for marking locations of focussed fluid migration on this margin.

Figure 9: Diagrammatic sketch of fluid expulsion at the Porangahau Ridge.

Figure A.1: Rock physics modelling of gas- and gas-hydrate-bearing sediments.
A: Conceptual distribution of gas and gas hydrates in a gas chimney. Dimensions and range of values for gas hydrate saturation (S_h) and free-gas saturation (S_g) from Liu and Flemings (2006). Sediments in the chimney contain a mix of gas and gas hydrates up to 40 m away from its axis, flanked by a 10-m thick wall with gas hydrates only. In the chimneys, 2-3% of free gas is predicted to coexist with 20-80%, mostly >50%, of gas hydrate.
B: Rock physics modelling, refer to Appendix A and Table A.1 for details. Predicted reflection coefficient from an interface between water-saturated sediments above sediments containing coexisting free gas and gas hydrates. Hydrate saturation S_h in the lower layer is 0 (only free gas), 0.4, and 0.7 of original porosity, gas saturation S_g is a fraction of original porosity, i.e., maximum gas saturation is 1-S_h. In the absence of gas hydrates and with even distribution of gas, gas saturation is predicted to be 7% in order to achieve a reflection coefficient of -0.25. For "patchy" gas distribution, a saturation of ~70% would be needed for a reflection coefficient of -0.25. A layer with coexisting gas and hydrates with S_g =2-3% and S_h >50%, as predicted in most models

by Liu and Flemings (2006), is unlikely to generate strong negative-polarity reflections.

Figure B.1: Depth error introduced by using the empirical TWT-depth function in (Townend, 1997a) at locations where velocity-depth functions were determined along Line 05CM-38 (Crutchley, 2009). Labels are equivalent locations in km along Line P6 (Figure 2), which coincides with Line 05CM-38. Negative value means depth is underestimated by using the empirical TWT-depth function. s-bsf: s beneath the seafloor. Undisturbed BSR and upwarped BGHS mark TWT to BSR and shallowest part of the high-amplitude zone, respectively.

Figure C.1: Thermal gradient along Line P6 assuming hydrostatic (hydro, as in Figure 5), lithostatic pressure (litho), and a natural-gas mix (nat-gas) with hydrostatic pressure. The latter has a negligible effect.

Figure 1

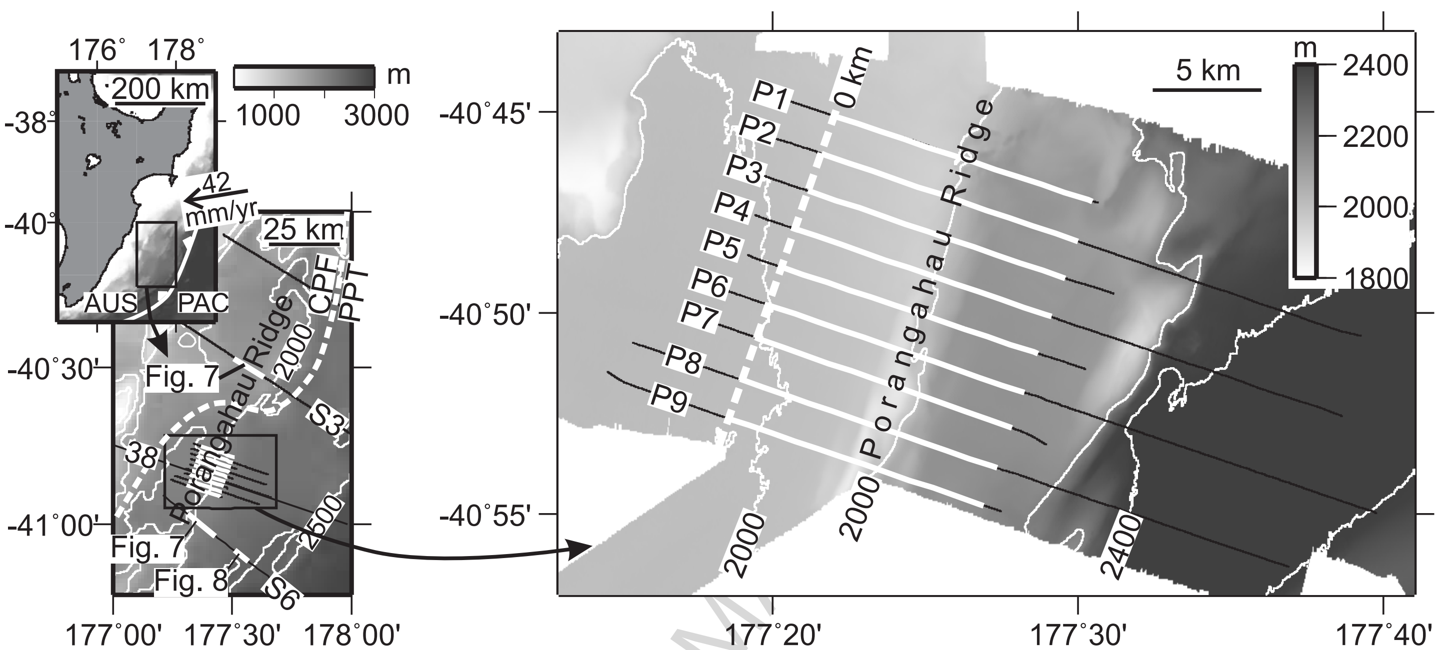

176˚
178˚
200 km
1000
3000
m
-38˚
-40˚
42
mm/yr
AUS
PAC
25 km
CPF
PPT
Porangahau Ridge
2000
Fig. 7
-40˚30'
S3
38
2500
-41˚00'
Fig. 7
Fig. 8
S6
177˚00'
177˚30'
178˚00'
-40˚45'
-40˚50'
-40˚55'
P1
P2
P3
P4
P5
P6
P7
P8
P9
0 km
5 km
m
2400
2200
2000
1800
2000
2000
2400
177˚20'
177˚30'
177˚40'

Figure 2 part 1 of 2 (tiff)

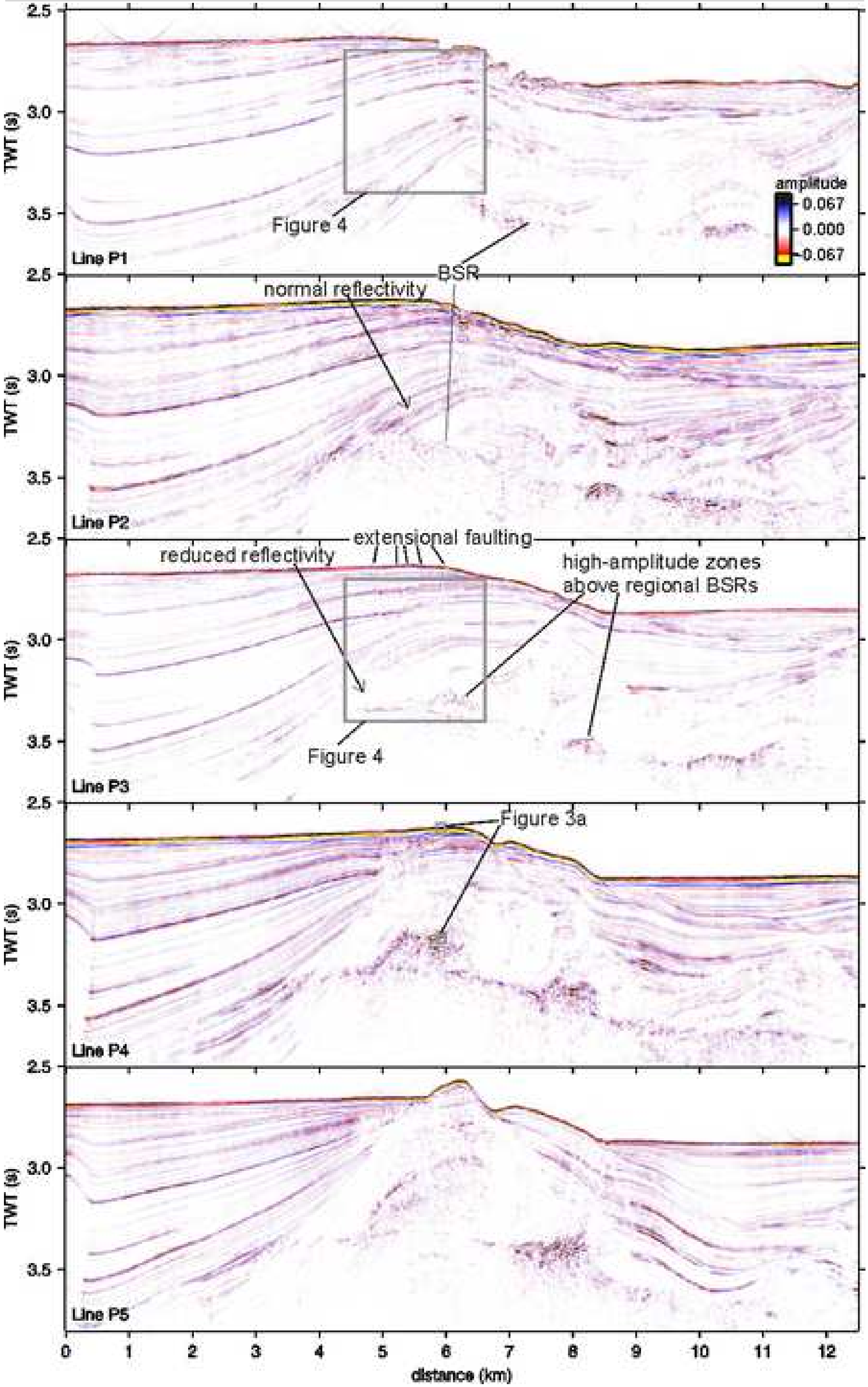

Figure 2 part 2 of 2 (tiff)

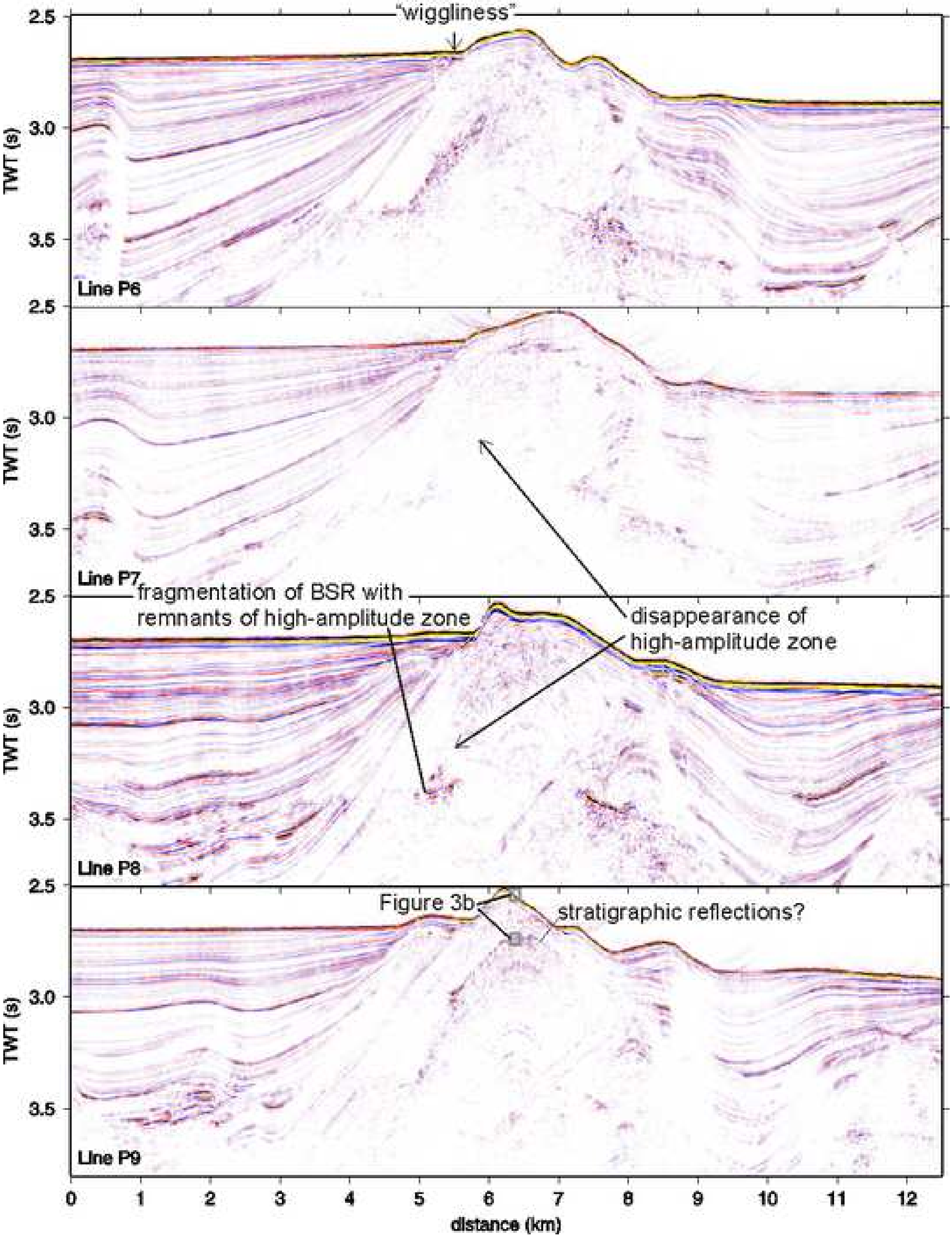

Figure 3

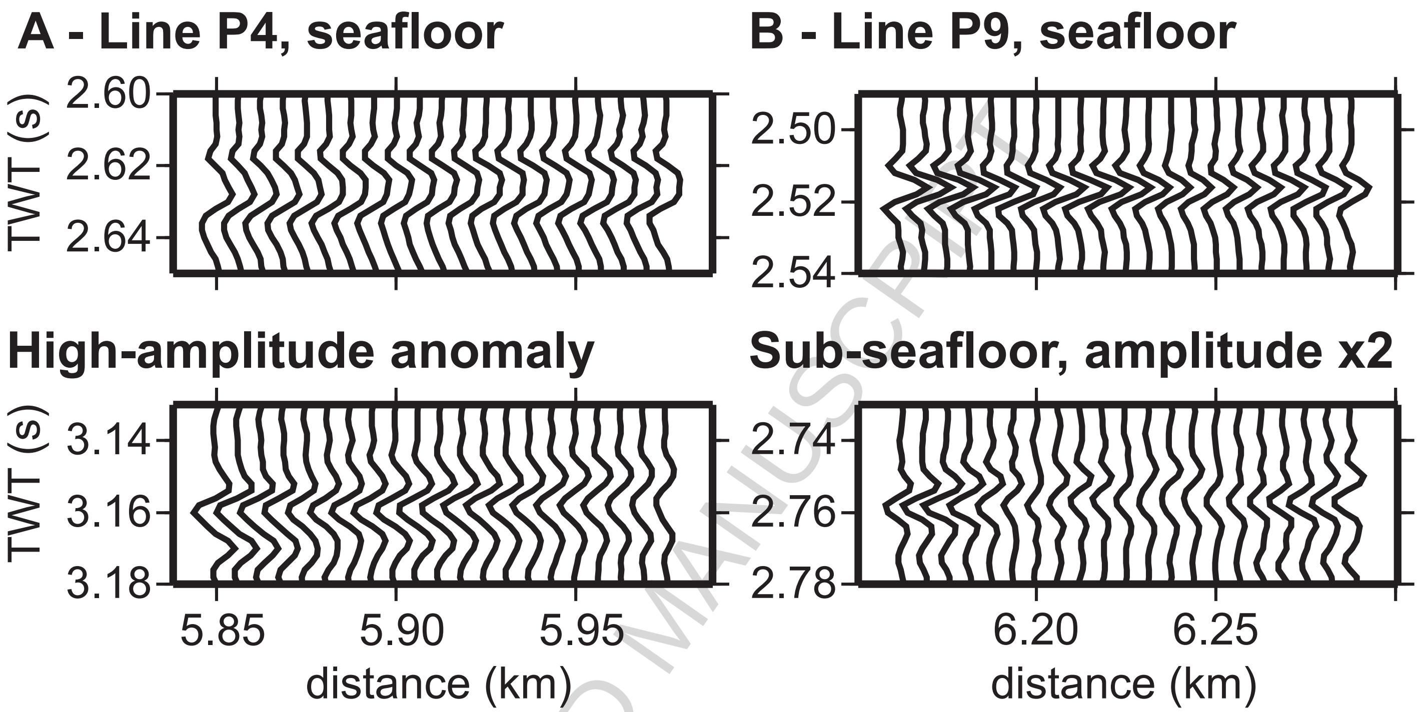

A - Line P4, seafloor
B - Line P9, seafloor
TWT (s)
2.60
2.62
2.64
2.50
2.52
2.54
High-amplitude anomaly
Sub-seafloor, amplitude x2
3.14
3.16
3.18
2.74
2.76
2.78
5.85
5.90
5.95
distance (km)
6.20
6.25
distance (km)

Figure 4

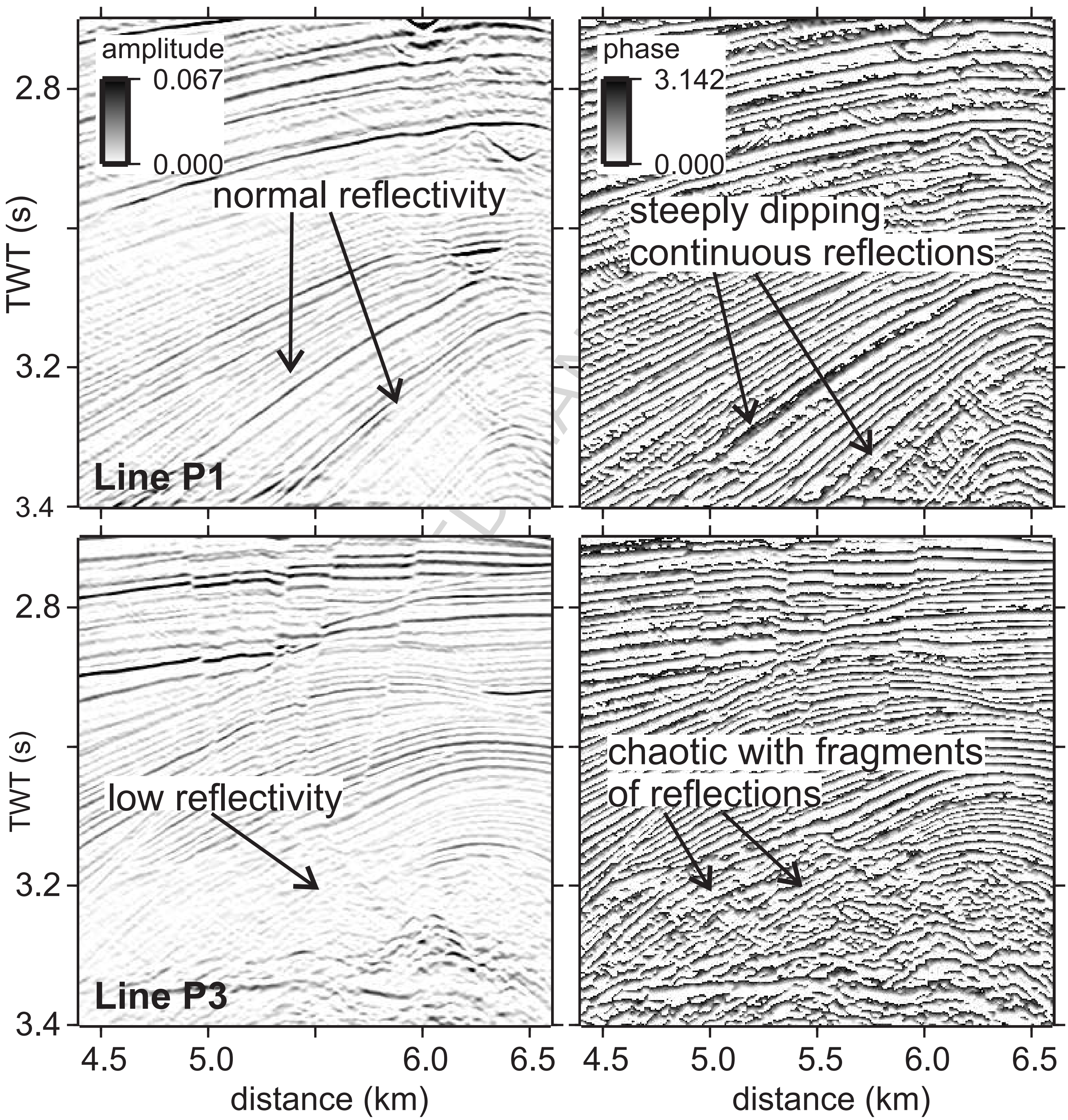
amplitude
0.067
0.000
normal reflectivity
Line P1
phase
3.142
0.000
steeply dipping, continuous reflections
low reflectivity
Line P3
chaotic with fragments of reflections
TWT (s)
2.8
3.2
3.4
4.5
5.0
5.5
6.0
6.5
distance (km)

Figure 5

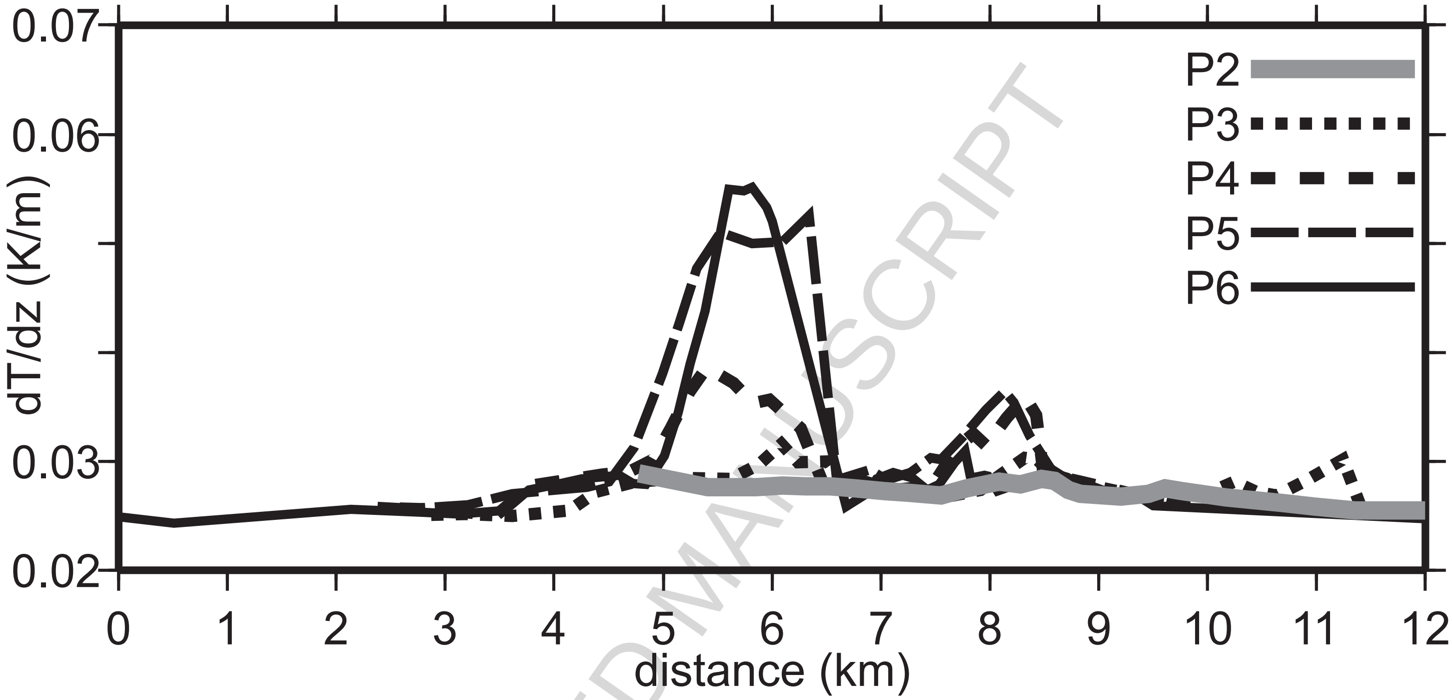
0.07
0.06
0.03
0.02
dT/dz (K/m)
0 1 2 3 4 5 6 7 8 9 10 11 12
distance (km)
P2
P3
P4
P5
P6
ACCEPTED MANUSCRIPT

Figure 6

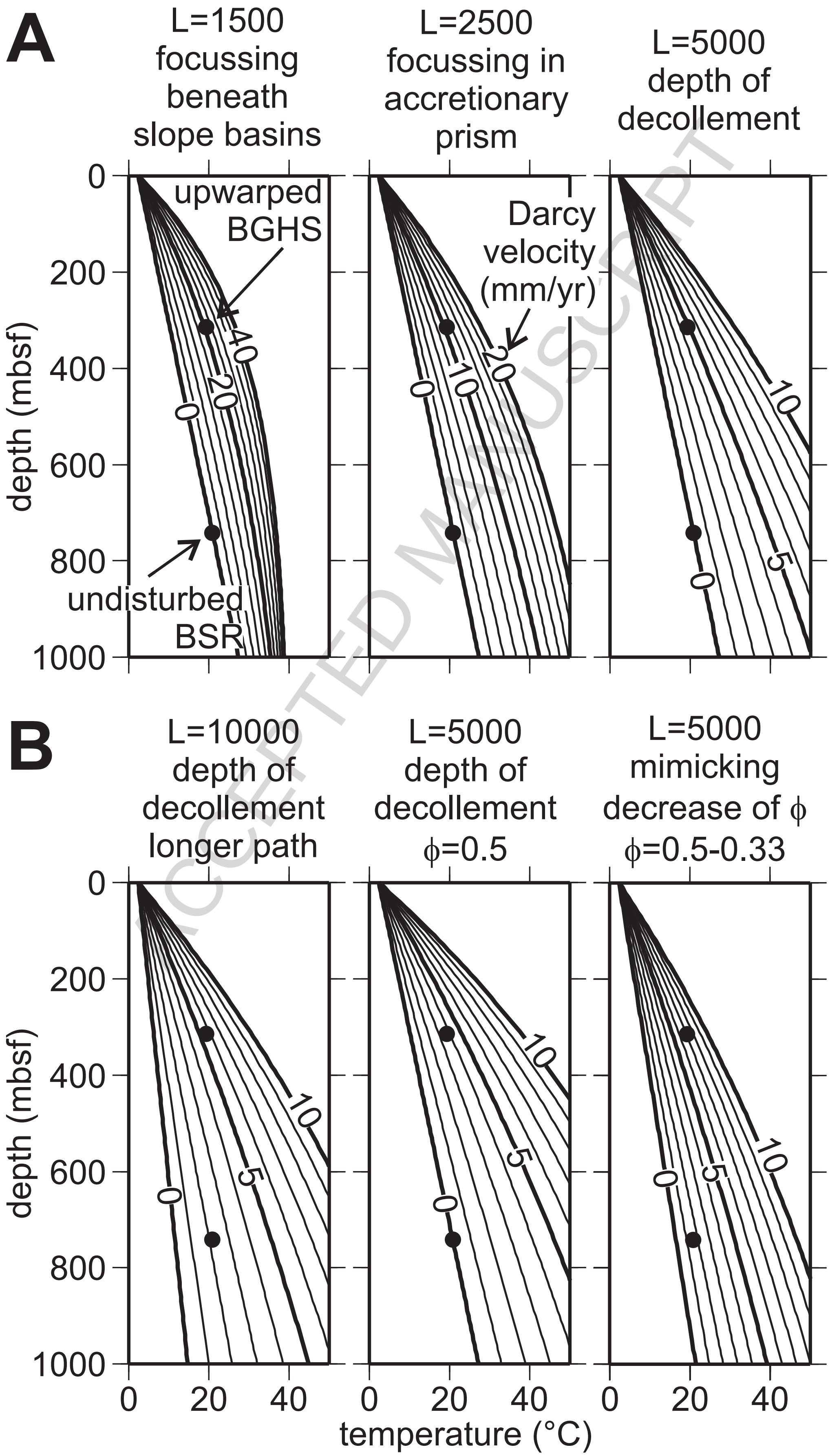
A
L=1500
focussing
beneath
slope basins
L=2500
focussing in
accretionary
prism
L=5000
depth of
decollement
upwarped
BGHS
Darcy
velocity
(mm/yr)
undisturbed
BSR
40
20
0
20
10
0
10
5
0
depth (mbsf)
0
200
400
600
800
1000
B
L=10000
depth of
decollement
longer path
L=5000
depth of
decollement
ϕ=0.5
L=5000
mimicking
decrease of ϕ
ϕ=0.5-0.33
10
5
0
10
5
0
10
5
0
depth (mbsf)
0
200
400
600
800
1000
0
20
40
temperature (°C)

Figure 7

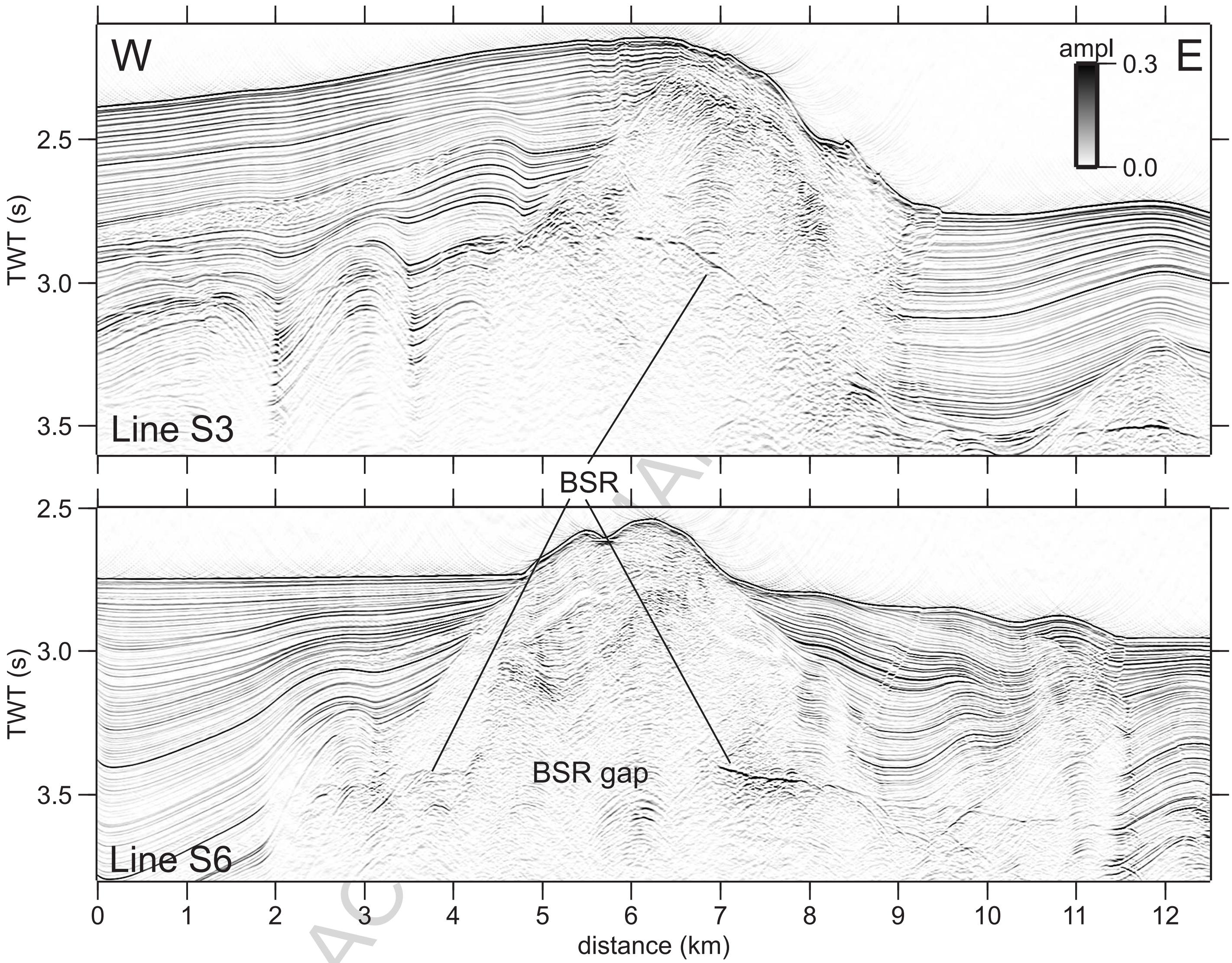
W
E
ampl
0.3
0.0
TWT (s)
2.5
3.0
3.5
Line S3
BSR
TWT (s)
2.5
3.0
3.5
BSR gap
Line S6
0
1
2
3
4
5
6
7
8
9
10
11
12
distance (km)

Figure 8

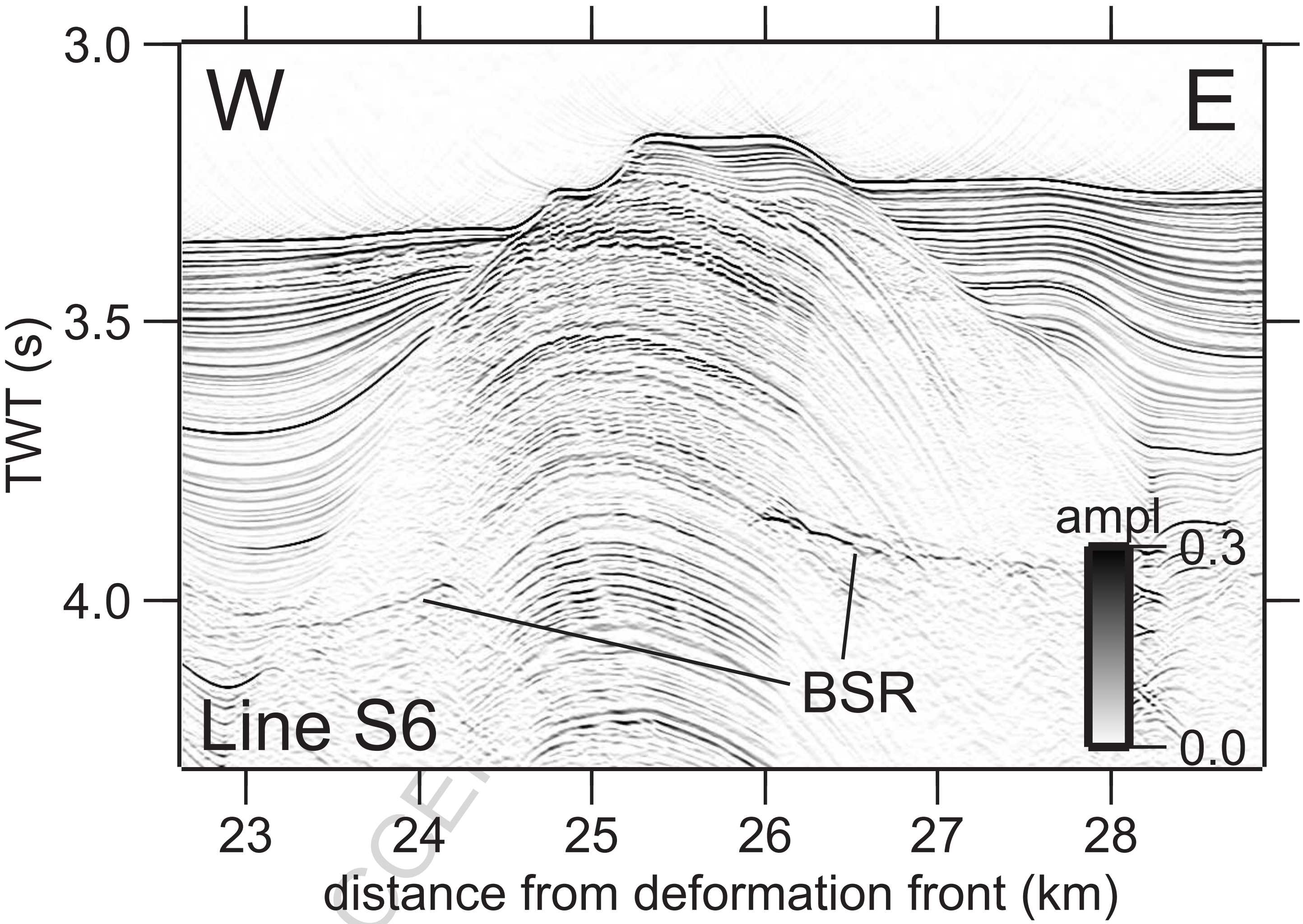

3.0
3.5
4.0
TWT (s)
W
E
ampl
0.3
0.0
BSR
Line S6
23
24
25
26
27
28
distance from deformation front (km)

Figure 9

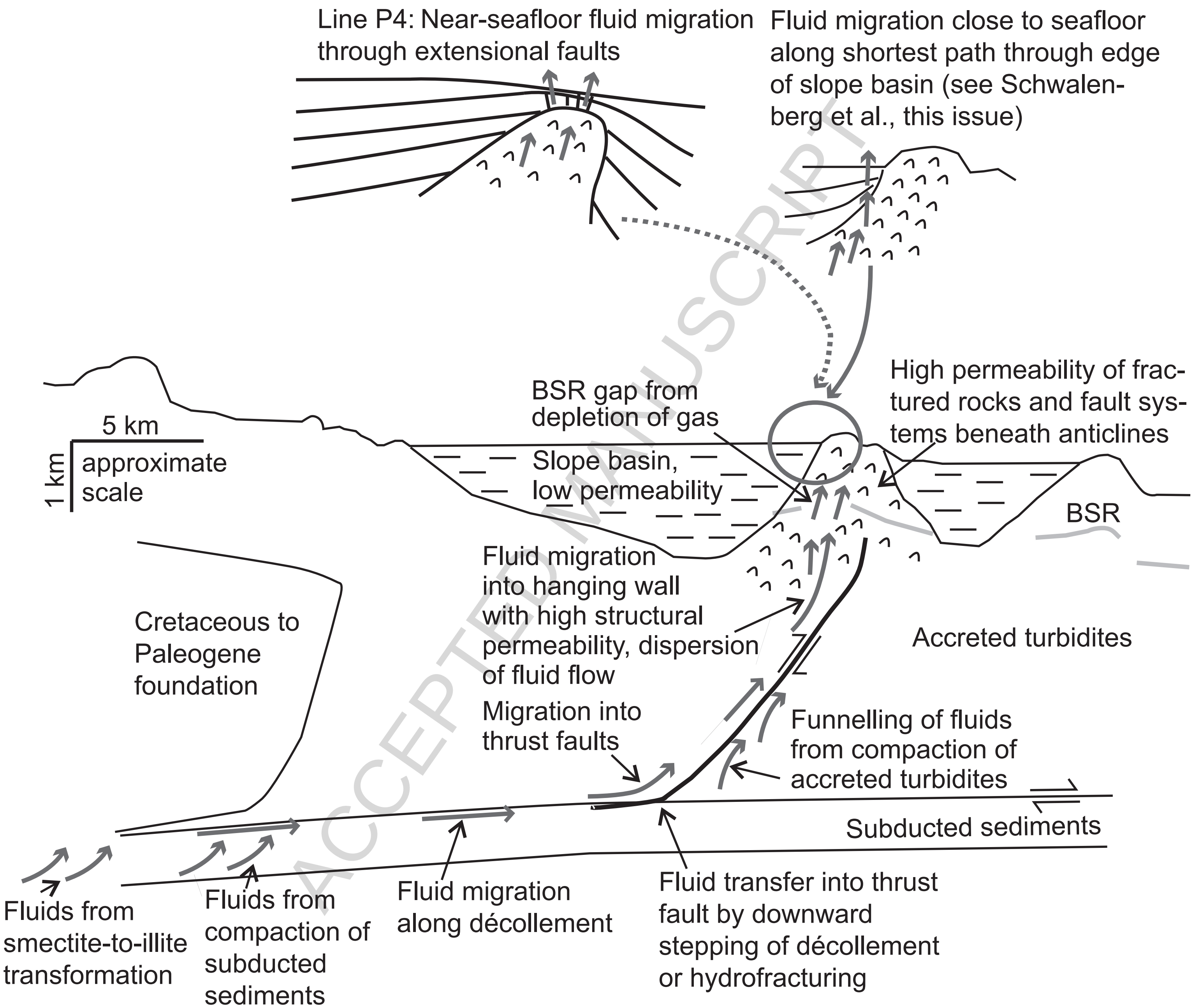

Line P4: Near-seafloor fluid migration through extensional faults
Fluid migration close to seafloor along shortest path through edge of slope basin (see Schwalenberg et al., this issue)
5 km
1 km
approximate scale
BSR gap from depletion of gas
Slope basin, low permeability
High permeability of fractured rocks and fault systems beneath anticlines
BSR
Cretaceous to Paleogene foundation
Fluid migration into hanging wall with high structural permeability, dispersion of fluid flow
Accreted turbidites
Migration into thrust faults
Funnelling of fluids from compaction of accreted turbidites
Subducted sediments
Fluids from smectite-to-illite transformation
Fluids from compaction of subducted sediments
Fluid migration along décollement
Fluid transfer into thrust fault by downward stepping of décollement or hydrofracturing

Figure A.1

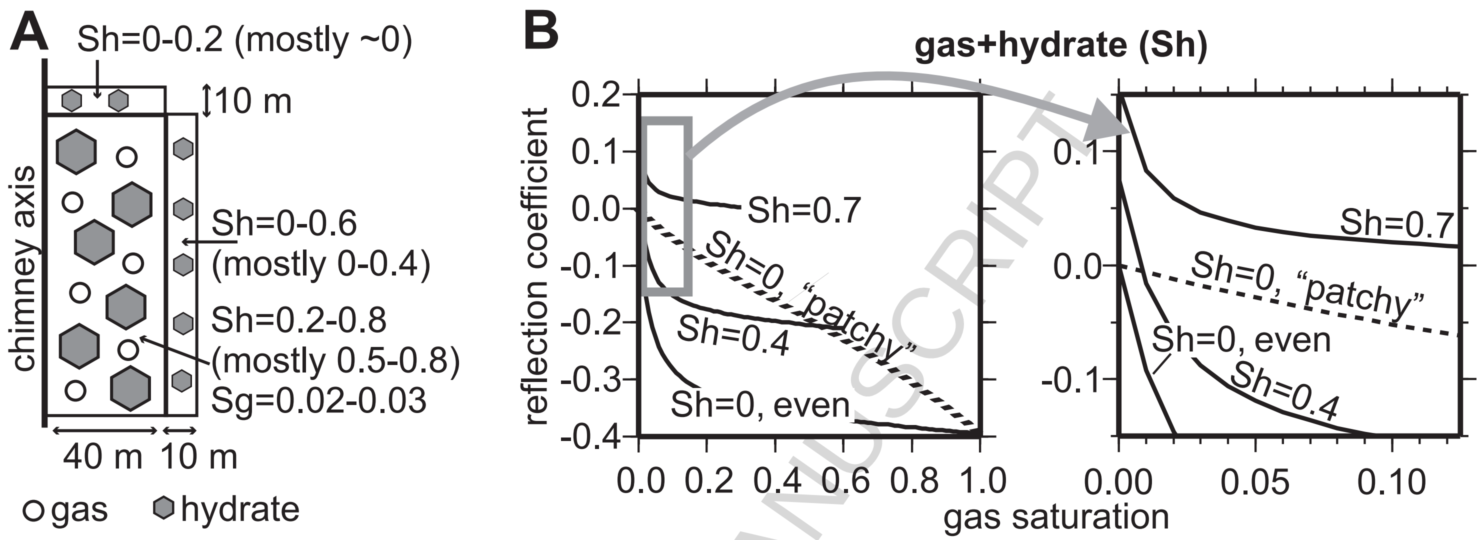
A
Sh=0-0.2 (mostly ~0)
10 m
chimney axis
Sh=0-0.6
(mostly 0-0.4)
Sh=0.2-0.8
(mostly 0.5-0.8)
Sg=0.02-0.03
40 m
10 m
gas
hydrate
B
gas+hydrate (Sh)
reflection coefficient
0.2
0.1
0.0
-0.1
-0.2
-0.3
-0.4
Sh=0.7
Sh=0, "patchy"
Sh=0.4
Sh=0, even
0.0
0.2
0.4
0.6
0.8
1.0
gas saturation
0.00
0.05
0.10

Figure B.1

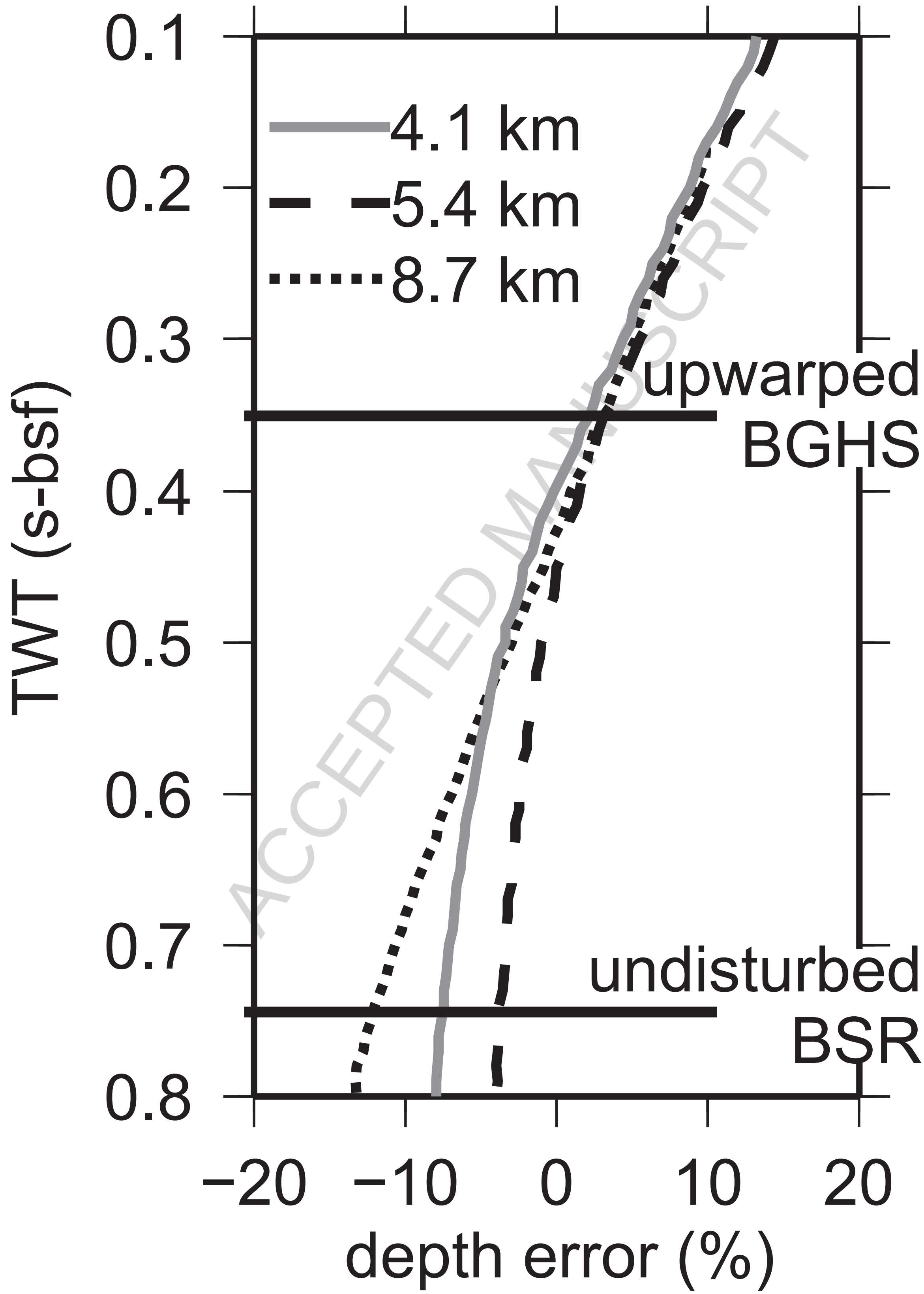

4.1 km
5.4 km
8.7 km
upwarped
BGHS
undisturbed
BSR
0.1
0.2
0.3
0.4
0.5
0.6
0.7
0.8
TWT (s-bsf)
−20
−10
0
10
20
depth error (%)

Figure C.1

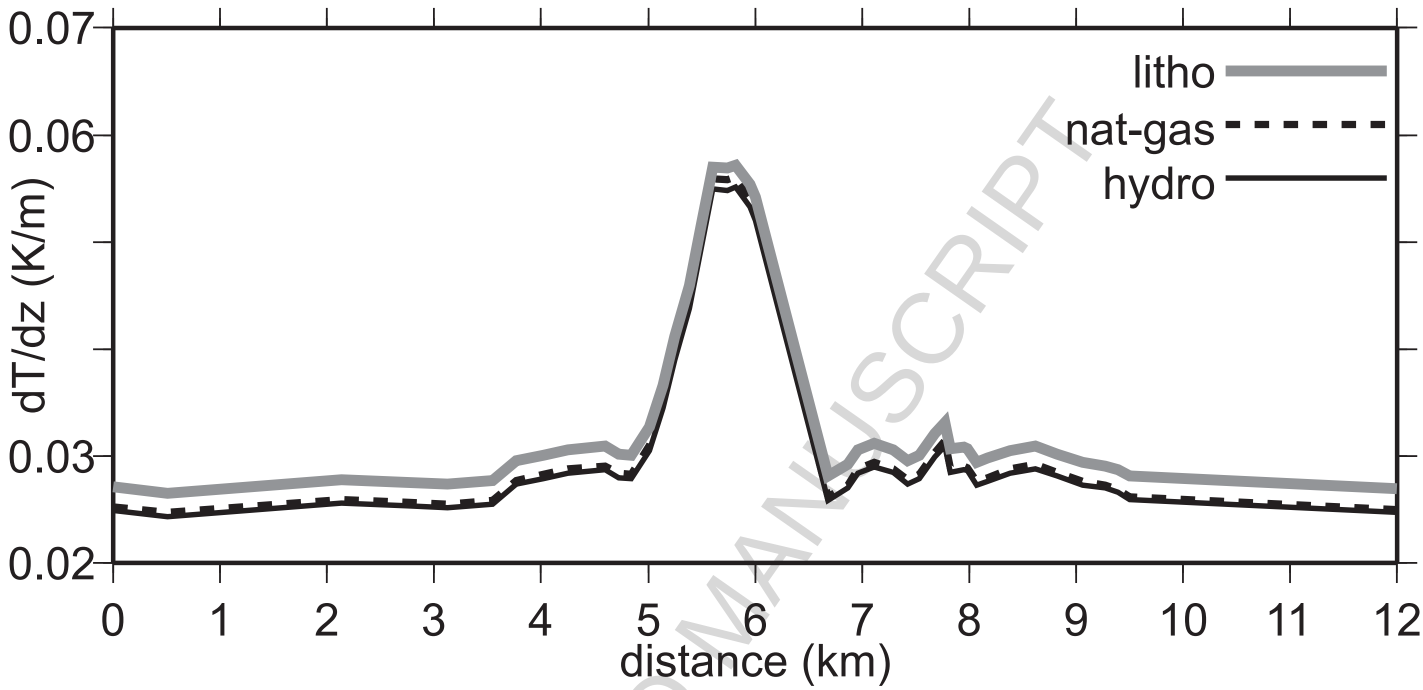

0.07
0.06
0.03
0.02
dT/dz (K/m)
0
1
2
3
4
5
6
7
8
9
10
11
12
distance (km)
litho
nat-gas
hydro

Table 1: Acquisition parameters. Additional parameters: Source depth: 5 m. Shot interval: 10.8 s. Vessel speed: 4-5 knots through water. Near-offset: 40 m. Group spacing: 12.5 m. Sampling rate: 0.5 s. Original numbering of lines as in Pecher et al. (2007). Streamer depth varied because of weather conditions.

Line	Original no.	No. of channels	Far offset (m)	Streamer depth (m)
P1	21	40	448.75	5
P2	04	32	548.75	7.5
P3	20	24	448.75	5
P4	03	32	548.75	7.5
P5	19	24	448.75	5
P6	02	32	548.75	7.5
P7	18	24	448.75	5
P8	01	32	648.75	10
P9	17	24	448.75	5

Table 2: Input parameters for constraining advective heatflow. K_f and K_g are commonly used values (e.g., Minshull and White, 1989), matching those in Townend (1997a). C_f is commonly used for water (e.g., Xu and Ruppel, 1999).

$T(0)$ (°C):	2.4
dT/dz (K/m):	0.025
ϕ:	0.33
K_f (W m^{-1} K^{-1}):	0.6
K_g (W m^{-1} $K^{-}1$):	2.8
C_f (J kg^{-1} C^{-1}):	4180
ρ_f (kg/m^3):	1035

Table A.1: Parameters used for rock physics modelling. Fraction: fraction of frame material, excluding hydrate. We varied the fraction of clay to match predicted velocities at 474 mbsf, porosity is derived from that velocity (Hamilton, 1978). K: compressional modulus, μ: shear modulus, ρ: density. Elastic constants for clay and SiO_2 are from Helgerud et al. (1999) and references therein. Hydrate properties after Waite et al., (1998), gas properties for methane (Gray, 1972) at the predicted pressure-temperature conditions. Critical porosity and coordination number are commonly used values for sands (Mavko et al., 1998), providing a measure of how the randomly packed spheres are connected.

Porosity:	0.41
Confining pressure (MPa):	27.80
Pore pressure (MPa):	24.42
Temperature (K):	293.18
Coordination number:	9
Critical porosity:	0.36

Components:

	Clay	SiO_2	Hydrate	Water	Gas
Fraction	0.12	0.88	-	-	-
K (GPa)	20.90	37.00	7.70	2.32	0.027
μ (GPa)	6.85	44.00	3.21	0	0
ρ (kg/m^3)	2580	2650	910	1030	190

Table E.1: Estimate of fluid volumes entering and expelled from subduction zone. Input values were estimated as follows:

[1]Thickness of incoming section: TWT above and below décollement from Line SO-191-6 (Barnes et al., this issue) seawards of the deformation front and the TWT-depth function in Appendix B (Townend, 1997a).

[2]Porosity of incoming sediments: Approximate averages from Ocean Drilling Program Leg 190 Sites 1173 and 1174, which were drilled about 10 km seaward and 2 km landward of the deformation front, respectively, in a similar setting on the Nankai Trough (Screaton et al., 2002).

[3]Final porosity of compacted sediments, smectite fraction, water fraction in smectite, values representative for other accretive setting (Moore and Vrolijk, 1992, in Townend, 1997b).

[4]Subduction velocity, corrected for obliquity (DeMets et al., 1994; Henrys et al., 2006).

[5]Subduction velocity in Townend (1997b) from Beanland (1992).

	This study	Townend (1997b)
h_{accr} (m)	2200[1]	1500
h_{sub} (m)	900[1]	-
ϕ_{accr}	0.55[2]	0.40
ϕ_{comp}	0.10[3]	0.10[3]
ϕ_{sub}	0.35[2]	-
v (m/yr)	0.035[4]	0.04[5]

S	0.20[3]	0.20[3]
W	0.35[3]	0.35[3]
V_{accr} (m^3 yr-1 m^{-3})	42	24
V_{comp} (m^3 yr-1 m^{-3})	39	20
V_{hydac} (m^3 yr-1 m^{-3})	2.4	3
V_{sub} (m^3 yr-1 m^{-3})	11	-
V_{hydsub} (m^3 yr-1 m^{-3})	1.4	-